

Low-frequency-selected Fast Radio Burst Host Galaxy Candidates

Y.-Z. Sun,¹ R. L. C. Starling,¹ R. A. J. Eyles-Ferris,¹ A. Rowlinson,^{2,3} R. A. M. J. Wijers,^{2,3} N. R Tanvir¹

¹School of Physics and Astronomy, University of Leicester, University Road, Leicester, LE1 7RH, UK

²Anton Pannekoek Institute for Astronomy, University of Amsterdam, Science Park 904, 1098 XH, Amsterdam, The Netherlands

³ASTRON, the Netherlands Institute for Radio Astronomy, Oude Hoogeveensedijk 4, 7991 PD, Dwingeloo, The Netherlands

Accepted XXX. Received YYY; in original form ZZZ

ABSTRACT

We present a pilot study on the host galaxy environments of CHIME/FRBs by cross-matching baseband-localised events with the LOFAR Two-metre Sky Survey Data Release 2 (LoTSS DR2) at 144 MHz. Unlike traditional methods reliant on optical imaging, our radio-based selection allows for the identification of dust-obscured or optically faint star-forming galaxies. Of the 140 CHIME FRBs considered, 33 lie within the LoTSS DR2 footprint, and 16 show potential radio counterparts. Through multi-wavelength analysis, spectral energy distribution (SED) fitting, and redshift constraints from the Macquart relation, we identify two secure and one tentative host candidates, all consistent with active star formation. However, their H α -derived star formation rates appear underestimated, likely due to significant dust attenuation, as suggested by infrared colours and compact optical morphologies. Our results highlight the value of low-frequency radio data in complementing optical host searches and demonstrate the feasibility of host identification even in the absence of optical confirmation. With forthcoming data from LoTSS DR3 and the full CHIME/FRB baseband release, this method offers a promising path toward statistically robust studies of FRB host galaxies and their environments.

Key words: fast radio bursts - radio continuum: galaxies - galaxies: star formation

1 INTRODUCTION

Fast radio bursts (FRBs) are a class of millisecond-duration radio transients of extragalactic origin, as inferred from their large dispersion measures (DMs) along the line of sight. These events are extremely powerful, with typical bursts releasing $\sim 10^{38}$ – 10^{40} erg in just a few milliseconds, making FRBs among the most luminous radio phenomena in the Universe. The observed frequency range of FRBs spans widely, from about 110 MHz up to beyond 5.2 GHz (Pleunis et al. 2021; Gajjar et al. 2018). Over the past decade, large-scale surveys such as the Canadian Hydrogen Intensity Mapping Experiment (CHIME; CHIME/FRB Collaboration et al. 2018), the Commensal Radio Astronomy FAST Survey (CRAFTS; Niu et al. 2021), and the Commensal Real-time ASKAP Fast Transients Survey (CRAFT; James et al. 2019) have detected more than thousand FRBs.

The first FRB to be discovered, FRB 20010724A, was detected by Lorimer et al. (2007) as a single bright pulse. The extreme luminosities and short durations of FRBs point to compact object progenitors, most notably magnetically powered neutron stars (magnetars). This connection is strongly supported by the detection of FRB 20200428A, an FRB-like burst from the Galactic magnetar SGR 1935+2154 (Bochenek et al. 2020), supporting the idea that at least a fraction of FRBs are powered by magnetars. However, the localisation of FRB 20200120E to a globular cluster in M81 (Kirsten et al. 2022) challenges this paradigm, as such environments lack recent star formation and massive stars. Instead, FRB 20200120E

is thought to originate from a newly formed neutron star within an old stellar population, produced through alternative channels such as the accretion-induced collapse of a white dwarf or the merger of compact objects. These contrasting cases suggest that multiple formation pathways, linked to both young and old stellar populations, may contribute to the observed FRB population. Roughly 2.6 per cent of FRBs have been confirmed to repeat, although statistical models suggest that the true repeating fraction may be higher, due to limitations in observational cadence and sensitivity (Spitler et al. 2016; Chime/Frb Collaboration et al. 2023; Kirsten et al. 2024; Yamasaki et al. 2024).

Beyond their origin, FRBs also serve as powerful astrophysical probes. Their large DMs trace the integrated column of free electrons, offering unique insights into the ionised medium along the line of sight – including the Milky Way, its halo, and the intergalactic medium (IGM). Notably, Macquart et al. (2020) demonstrated that by using localised FRBs to estimate the average density of diffuse intergalactic gas, the long-standing problem of the Universe’s ‘missing baryons’ can be resolved, underscoring the potential of FRBs as valuable cosmological probes.

Despite their exceptional brightness and short durations in the radio band, confirmed counterparts of extragalactic FRBs at other wavelengths are extremely rare. A number of multi-wavelength follow-up campaigns have targets FRBs, searching for associated emission in the optical, X-ray, and gamma-ray bands, either contemporaneously with or shortly after radio bursts, but have resulted in non-detections. For example, Scholz et al. (2017) conducted simultaneous radio and X-ray observations of the repeating FRB

* E-mail: ys400@le.ac.uk

20121102A, detecting multiple radio bursts without any associated X-ray signal. Similarly, [Núñez et al. \(2021\)](#) used the Las Cumbres Observatory global telescope network to search for optical transients associated with eight well-localised FRBs, but found no counterparts. Only two tentative associations between FRBs and other high-energy transients have been reported. One links FRB 20190425A to the gravitational-wave event GW190425, a binary neutron star merger detected by LIGO/Virgo, with a chance alignment probability of only 0.52 percent ([Moroianu et al. 2023](#)). However, this association has since been rebutted and is no longer considered viable ([Magaña Hernandez et al. 2024](#)). Another connects FRB 20171209A to the host galaxy of GRB 110715A, with a matching redshift ([Wang et al. 2020](#)). While intriguing, both cases lack firm confirmation and highlight the need for larger samples.

The physical origins of FRBs remain one of the most fundamental open questions in modern astrophysics. Due to the extremely short durations of the bursts and the lack of persistent multi-wavelength counterparts, directly identifying progenitor systems remains observationally unfeasible. As a result, studying the host galaxies of FRBs has become a crucial approach to constraining their nature. Host properties, such as star-formation rate (SFR), stellar mass, morphology, and environment, can provide indirect but valuable clues about the types of systems capable of producing FRBs.

One statistical approach involves investigating whether FRBs preferentially occur in galaxies with high SFRs or high stellar masses ([Chatterjee et al. 2017; Mannings et al. 2021; Bhandari et al. 2022; Gordon et al. 2023; Sharma et al. 2024; Loudas et al. 2025](#)). While not a definitive test of progenitor type, such correlations can offer insight into the typical ages and evolutionary histories of FRB-producing populations. A trend with SFR would favour progenitors linked to young, massive stars and their remnants (e.g. magnetars formed in core-collapse supernovae), whereas a stronger dependence on stellar mass would suggest origins tied to older stellar populations or dynamical channels, such as neutron star mergers or accretion-induced collapse. For a comprehensive review of potential progenitor models, see [Zhang \(2023\)](#).

The diversity of FRB host galaxies has become increasingly apparent through case studies of individual localised sources. For example, the first repeating FRB 20121102A, is hosted by a low-metallicity, star-forming dwarf galaxy ([Tendulkar et al. 2017](#)), while FRB 20180924B and FRB 20190523A reside in massive, quiescent galaxies with little or no current star formation ([Bannister et al. 2019; Ravi et al. 2019](#)). By contrast, the repeating FRB 20190711A is associated with a moderately star-forming disk galaxy ([Heintz et al. 2020](#)). These examples indicate that FRBs can occur in a wide range of galactic environments.

This diversity has been confirmed by recent statistical studies. [Gordon et al. \(2023\)](#) analysed 23 FRB host galaxies and found a diversity of properties, with most residing in star-forming environments but some hosted by more quiescent galaxies. Similarly, [Horowitz & Margalit \(2025\)](#) argued that the FRB rate scales with both stellar mass and star formation, resembling trends seen in Type Ia supernovae. This view is supported by [Loudas et al. \(2025\)](#), who found that while many FRBs occur in star-forming galaxies, a non-negligible fraction are located in galaxies with relatively low star formation activity. Collectively, these findings suggest that FRBs may originate from multiple progenitor channels, and host galaxy studies will remain essential to disentangling their origins.

To date, over 100 FRB host galaxies have been identified ([Loudas et al. 2025](#)), the vast majority of which were recognised via optical observations. Interestingly, in four cases FRBs have been found to coincide with a persistent radio source (PRS) – a compact, long-

lived radio counterpart, much smaller than the host galaxy and thus indicative of the FRB’s local environment – that remains visible long after the burst, providing an additional clue to their origins ([Marcote et al. 2017; Chatterjee et al. 2017; Niu et al. 2022; Bhandari et al. 2023; Bruni et al. 2024a,b; Dong et al. 2024](#)). While PRSs such as that at the location of FRB 20121102 have provided valuable insight into the local environments of some repeaters, most FRBs lack any detectable persistent emission. VLBI observations confirmed that the bursts and the PRS of FRB 20121102A are co-located within tens of parsecs, and follow-up studies disfavour an AGN origin, instead supporting interpretations such as a plerionic nebula ([Marcote et al. 2017; Chen et al. 2023; Bhardwaj et al. 2025](#)). Long-term monitoring further shows that the PRS is compact, stable, and not directly correlated with burst activity. Another example is FRB 20190520B, the source is localized to a star-forming dwarf galaxy at $z = 0.241$ ([Niu et al. 2022; Chen et al. 2025](#)) and hosts a compact PRS constrained to a size of < 9 pc, co-located with the FRB to within ~ 80 pc ([Bhandari et al. 2023](#)), and exhibits a flat GHz spectrum with significant long-term variability ([Zhang et al. 2023](#)). Recent low-frequency observations reveal a spectral break attributed to absorption, pointing to a dense and magnetized local environment. These properties distinguish the PRS from star-formation-powered radio emission and make FRB 20190520B a benchmark system for compact FRB-associated PRSs ([Balasubramanian et al. 2025](#)). Furthermore, searches for radio emission from their host galaxies in existing continuum surveys have also frequently yielded non-detections, not necessarily because the galaxies lack radio emission, but likely due to insufficient survey depth or resolution. This motivates the use of deeper or lower-frequency radio data to explore whether more FRB hosts can be identified through their continuum radio emission.

In the absence of reliable radio detections, optical observations have become the primary method for host identification. However, this approach introduces its own selection biases. Faint or obscured host galaxies are less likely to be detected or confidently associated with FRBs, particularly when positional uncertainties are large. As a result, current host samples are biased toward more massive and actively star-forming galaxies. Additionally, [Bhardwaj et al. \(2024a\)](#) demonstrated that FRBs are more often detected in face-on galaxies than in edge-on systems, likely due to lower line-of-sight scattering, further contributing to host population bias. These limitations may cause an underestimation of the true diversity of FRB host galaxies.

The bias against detecting faint hosts skews the inferred properties of FRB host galaxies, leading to an over-representation of massive, star-forming systems while underestimating the fraction of low-mass or quiescent galaxies. Radio-based host identification provides a complementary approach by being less affected by dust obscuration, allowing for more reliable estimates of star-formation activity. However, radio selection is itself not free from bias: it remains more sensitive to galaxies with significant synchrotron emission, and may still miss radio-faint, quiescent hosts. Nonetheless, combining optical and radio-selected samples offers a more complete view of the FRB host population and helps to better characterise their underlying diversity ([Seebeck et al. 2021](#)).

In this study, we use the CHIME/FRB baseband localisation catalogue to identify candidate host galaxies through positional matches with LoTSS sources and assess their chance-coincidence probabilities (Section 2). We then estimate redshifts and derive physical properties using multi-wavelength data (Section 3), present the resulting host candidates, compare their properties with known samples (Section 4), discuss the limitations of our approach (Section 5), and conclude with a summary of our main findings (Section 6).

Throughout this paper we assume a flat Λ CDM cosmology with $H_0 = 70 \text{ km s}^{-1} \text{ Mpc}^{-1}$, $\Omega_m = 0.3$, and $\Omega_\Lambda = 0.7$.

2 CROSMATCHING AND CANDIDATE IDENTIFICATION

2.1 Sample

Our sample of FRBs was taken from the CHIME/FRBs baseband data (CHIME/FRB Collaboration et al. 2024). The Canadian Hydrogen Intensity Mapping Experiment Fast Radio Burst Project (CHIME/FRB) is a large-scale, real-time survey dedicated to the discovery and monitoring of fast radio bursts. Operating at frequencies between 400-800 MHz, CHIME/FRB utilises a stationary, wide-field interferometric radio telescope located in Penticton, British Columbia, Canada. The telescope’s large field of view (~ 200 square degrees) and continuous monitoring capability make it particularly well-suited for detecting transient events like FRBs.

Since starting full operations in 2018, CHIME/FRB has rapidly become the leading instrument in terms of the number of FRB discoveries. The CHIME/FRB Collaboration has published catalogues containing hundreds to thousands of bursts, including both one-off and repeating sources (CHIME/FRB Collaboration et al. 2021; Chime/Frb Collaboration et al. 2023). In its most recent data release, the Baseband FRB catalogue (CHIME/FRB Collaboration et al. 2024), the collaboration reported 140 FRBs, 12 of which originate from seven repeaters. The measurements of burst properties including position, dispersion measure (DM), flux, fluence, and exposure, have been significantly improved compared to CHIME/FRB’s first catalogue.

Compared to Catalogue 1, which relied on real-time total intensity detection pipelines and typically achieved localisation uncertainties on the order of several arcminutes, the Baseband Catalogue utilises raw voltage (baseband) to coherently reconstruct the FRB waveform. This allows for interferometric localisation with ten-arcsecond-level precision, representing an order-of-magnitude improvement in angular resolution. Such high spatial accuracy is crucial for unambiguous host galaxy associations, especially in crowded optical fields, and has enabled direct cross-identification with multi-wavelength surveys.

In addition to enhanced localisation, the baseband data offer microsecond time resolution and finer frequency channels, which together allow for more accurate measurements of scattering timescales, burst sub-structure, and polarisation. Overall, the Baseband Catalogue marks a significant advance in CHIME/FRB’s ability to characterise both the intrinsic and propagation properties of FRBs.

2.2 Crossmatching

To identify potential host galaxies of FRBs detected by CHIME/FRB, we cross-match their positions with deep low-frequency radio surveys. In particular, the LOFAR Two-metre Sky Survey (LoTSS) provides a powerful complementary dataset. LoTSS is a deep radio continuum survey conducted at 120-168 MHz using the LOFAR High Band Antennas (HBA), with the aim of imaging the entire northern sky with unprecedented sensitivity and angular resolution at low frequencies (Shimwell et al. 2017, 2019).

The second data release (LoTSS-DR2) covers over 5,700 square degrees and reaches a median sensitivity of $\sim 70 \mu\text{Jy}/\text{beam}$ with a resolution of 6 arcseconds, making it well-suited for detecting star-forming galaxies and AGN out to moderate redshifts. This resolution is comparable to, or better than the typical localisation accuracy

of CHIME/FRB baseband-detected sources, thus enabling reliable cross-identification. By matching CHIME/FRB baseband positions with LoTSS radio sources, we can associate FRBs with persistent radio counterparts, which are crucial for confirming host galaxies, estimating star formation activity, or identifying AGN.

We cross-matched the centroid positions of 140 CHIME/FRB baseband-detected events with the LoTSS DR2 source catalogue¹ to identify potential radio counterparts. Using the multi-order coverage (MOC) map provided by the LoTSS DR2 data release, we first determined which FRBs lie within the survey footprint. A total of 33 FRBs were found to be spatially covered by LoTSS (see Fig. 1).

For each FRB within the footprint, we queried the `lotss_dr2.main_sources` table using the `pyVO` package (Graham et al. 2014) to retrieve nearby LoTSS sources. The search region was defined as an ellipse centred on the FRB position, with semi-major and semi-minor axes equal to twice the reported 1σ uncertainties in right ascension and declination from the CHIME/FRB baseband catalogue, thereby corresponding to a 2σ localisation region. Any LoTSS source whose centroid lies within this elliptical 2σ region was recorded as a candidate counterpart.

A total of 27 LoTSS sources were identified within these search regions, associated with 16 unique FRBs. To exclude foreground stars, we cross-matched the radio source positions with the NASA/IPAC Extragalactic Database (NED) and SIMBAD using `astroquery` (Ginsburg et al. 2019), adopting a $10''$ search radius centred on each LoTSS source. Any source classified as stellar (e.g. with type ‘*’ or ‘Star’) was removed from the sample. The final list comprises 24 non-stellar radio sources linked to 16 CHIME FRBs, of which 15 are non-repeating and one is a confirmed repeater. In cases where multiple LoTSS sources were found within the elliptical region of a single FRB, we retained all candidate matches for subsequent analysis without applying additional selection criteria at this stage.

2.3 Chance Alignment Test

To evaluate the likelihood of physical association between the CHIME/FRB events and their candidate LoTSS counterparts, we estimated the probability of chance alignment using a Monte Carlo approach. We generated a reference sample of 15,000 random sky positions and selected only those with at least one LoTSS DR2 source located within a radius of 5 arcminutes, thereby ensuring they lie within the survey footprint.

For each valid random position, we measured the angular separations to all nearby LoTSS DR2 sources within 5 arcminutes. To characterise the nature of these sources, we cross-matched them with the NASA/IPAC Extragalactic Database (NED), assuming the LoTSS source corresponds to the nearest object within a 10-arcsecond matching radius. Sources classified as stellar were excluded, and only extragalactic objects were retained for further analysis.

To assess the statistical significance of the observed cross-matching results, we employed a two-dimensional kernel density estimation (KDE) method in the separation-flux space. The KDE models were constructed for both the random sample and the FRB-matched sample using the same kernel bandwidth. For the choice of the KDE kernel bandwidth, we adopt Scott’s rule as the baseline and apply a scaling factor of 0.1 to reduce oversmoothing and preserve the tail structure of the random-match distribution, which is critical for identifying significant outliers. The null hypothesis of this analysis is that the FRB and radio source are not physically associated

¹ https://lofar-surveys.org/dr2_release.html

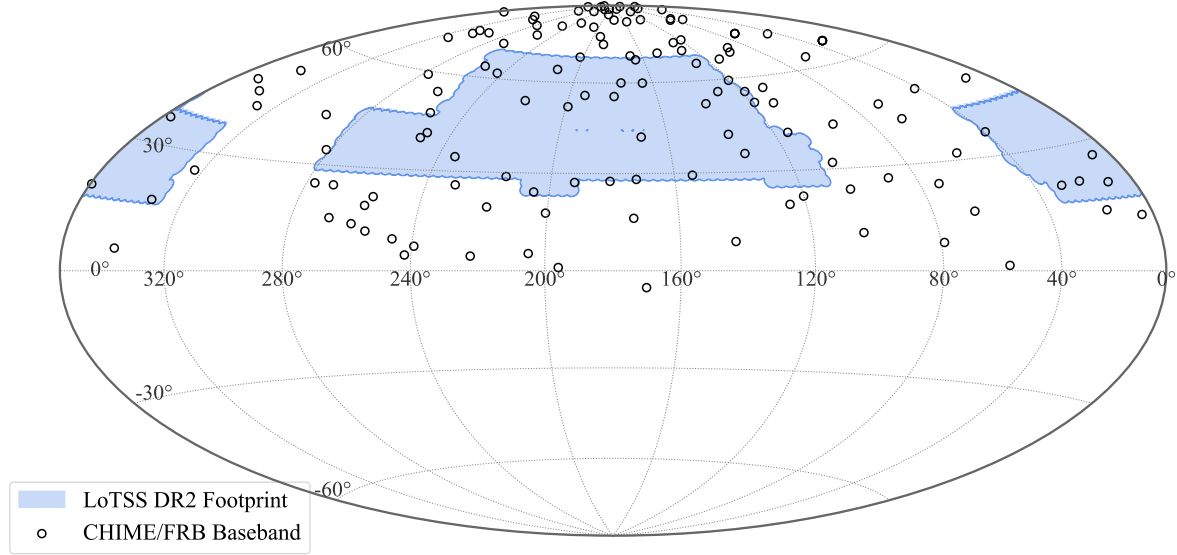


Figure 1. Sky distribution of 140 CHIME/FRB baseband-detected events (black circles) overlaid on the LoTSS DR2 survey footprint (shaded region). This figure illustrates which FRBs lie within the LoTSS coverage area based on the multi-order coverage (MOC) map. A total of 33 FRBs are found to fall within the footprint and are eligible for further cross-matching analysis.

and that any apparent association arises purely from random alignment with the background LoTSS source population. By comparing the resulting density distributions, we quantified deviations from the null hypothesis of random alignment.

Fig. 2 shows the KDE distributions for both datasets, with contours marking regions of increasing density. The outermost contour indicates the boundary enclosing 99.9 percent of random data. For each FRB-LoTSS pair, we evaluated its KDE-derived density under the random distribution model and calculated the probability of obtaining an equal or higher density by chance. This probability is a quantitative measure of statistical significance of each FRB-radio source association, with lower probabilities indicating a higher probability of physical association.

Based on the KDE chance-alignment analysis, we identified four candidate host galaxies with a chance probability below 0.1 percent. One of these corresponds to the known repeater FRB 20191106C, which has already been studied in detail in the literature and shown to be associated with an optical host galaxy (Ibik et al. 2024a,b). We therefore do not include it in our analysis here. The remaining three sources were retained as plausible hosts. We further classified them into two secure identifications and one tentative association, which are highlighted in Fig. 2 and will be discussed in Section 4. Table 1 shows the basic properties of the three candidates for the FRB host.

We also estimate the expected number of chance associations for our three candidates by randomly placing FRB error regions of the same size within the LoTSS DR2 footprint and counting how many LoTSS sources would fall within. This can be approximated using $N = \sum_{i=1}^3 \pi \theta_i^2 N_R / \Omega$, where N_R is the total number of LoTSS DR2 sources, Ω is the sky area covered by LoTSS DR2, and $\sum_{i=1}^3 \pi \theta_i^2$ represents the total area of the FRB error regions. All three candidates lie within a 1σ region of the FRB centre positions. Assuming a 1σ error region, the expected number of random crossmatches is ~ 0.86 . This implies that, statistically, less than one of the three candidates is likely to be a false association.

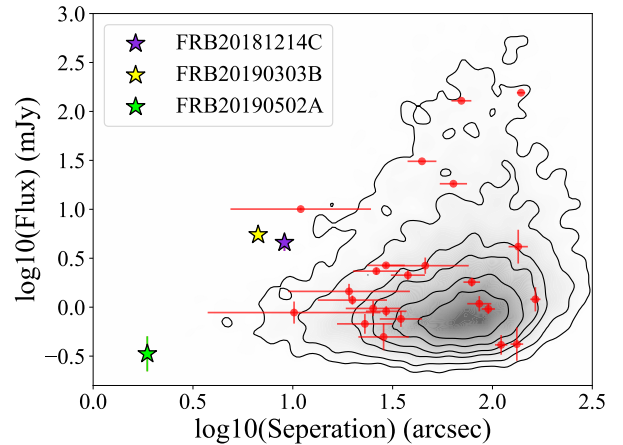


Figure 2. The correlation between FRB–radio-source separation and flux density for non-star objects in the LoTSS DR2 release. Coloured stars mark significant outliers from the random distribution, identified based on the KDE chance-alignment analysis and suggesting a higher likelihood of being the true host. Grey shade indicates density of matches to 15000 random points, and black contours, from the outermost to the innermost, represent the cumulative distributions of 99.9%, 99%, 95%, 90%, 75%, and 50% of the random points, respectively. Red points represent the matched FRBs, with error bars indicating the spatial extent of each radio galaxy.

3 HOST ANALYSIS METHODS

3.1 Redshift Estimation

The dispersion measure (DM) quantifies the integrated column density of free electrons along the line of sight between the FRB source and the observer. It is defined as $DM = \int_0^D n_e(l) dl$, where $n_e(l)$ is the free electron density (in cm^{-3}) at a distance l (in parsecs) along the line of sight. The resulting DM has units of pc cm^{-3} , and higher DM values generally indicate longer path lengths through ionised media or regions with a higher plasma density.

For extragalactic FRBs, the total observed dispersion measure DM_{FRB} is typically separated into three main contributions:

$$\text{DM}_{\text{FRB}} = \text{DM}_{\text{MW}} + \text{DM}_{\text{cosmic}} + \frac{\text{DM}_{\text{host}}}{(1 + z_{\text{FRB}})}, \quad (1)$$

where DM_{MW} includes the Milky Way disk and halo contributions, DM_{host} represents the host galaxy and local environment, and $\text{DM}_{\text{cosmic}}$ accounts for the contribution from the intergalactic medium (IGM). The DM_{MW} component was estimated using the YMW16 Galactic electron density model (Yao et al. 2017) for the disk, and a fixed halo contribution of 30 pc cm^{-3} (Dolag et al. 2015), as adopted by the CHIME/FRB Collaboration (CHIME/FRB Collaboration et al. 2024).

To estimate redshifts, we adopted the central DM–redshift relation between $\text{DM}_{\text{cosmic}}$ and redshift proposed by Macquart et al. (2020) (see their Fig. 2), assuming a host contribution of $50(1+z)^{-1} \text{ pc cm}^{-3}$ (Arcus et al. 2021; Bernales-Cortes et al. 2025), with redshift uncertainties estimated from the intrinsic scatter (central 90 percent range) of the relation. In addition, we considered the probabilistic modelling of the DM– z relation from Tang et al. (2023), which accounts for IGM fluctuations and host uncertainties via a Bayesian inference framework calibrated with a sample of FRBs with known redshifts.

3.2 Host Galaxy Characterisation

3.2.1 Spectral Energy Distribution Fitting

To investigate the physical nature of the candidate host galaxies, we performed spectral energy distribution (SED) fitting using publicly available optical and infrared photometry. The multi-wavelength data were retrieved via the VizieR catalogue service and compiled from several archival surveys, including Galaxy Evolution Explorer (GALEX) in the ultraviolet (Bianchi et al. 2011), Sloan Digital Sky Survey (SDSS) DR16 in the optical (Ahumada et al. 2020), Two Micron All-Sky Survey (2MASS) in the near-infrared (Skrutskie et al. 2006), Wide-field Infrared Survey Explorer (WISE) in the mid-infrared (Cutri et al. 2013), and Herschel in the far-infrared (Herschel Team et al. 2024) when accessible. A detailed description of the photometric measurements adopted from each survey is provided in Appendix A. These data were used to derive key galaxy properties such as stellar mass, star formation rate (SFR), dust attenuation, and stellar age. Not all sources are covered by all surveys; however, for each galaxy we include all available photometric measurements in the SED fitting. Prior to SED fitting, observed photometric fluxes were corrected for foreground Galactic extinction. The colour excess $E(B-V)$ at each source position was obtained from the Schlegel–Finkbeiner–Davis (SFD) dust map (Schlegel et al. 1998), and the extinction correction was applied using the extinction law of Cardelli et al. (1989) with $R_V = 3.1$.

The SED fitting was carried out using the CIGALE code (Boquien et al. 2019), adopting the `sfh2exp` star formation history module. This model consists of an old stellar population and a secondary burst, both characterised by exponentially declining star formation rates with independent ages and e-folding times. The mass fraction of the burst component was allowed to vary to account for recent star formation activity.

Stellar emission was modelled using the templates from Bruzual & Charlot (2003) with a Salpeter (1955) initial mass function. The stellar metallicity was allowed to vary over two representative values (sub-solar and solar) to account for plausible variations among the host galaxies. Nebular emission, including both line and continuum components, was included with a fixed ionisation parameter

and gas-phase metallicity. These nebular parameters were fixed to reduce degeneracies with other SED parameters, given the limited number of emission-line and ultraviolet constraints available for our sources, and because they have a negligible impact on the broadband-derived stellar masses and star formation rates. Dust attenuation was implemented via a modified power-law attenuation law, allowing for differential extinction between young and old stellar populations. Infrared dust re-emission was modelled following Draine & Li (2007), with free parameters for the polycyclic aromatic hydrocarbons (PAH) fraction and the interstellar radiation field intensity.

A Bayesian analysis was used to explore the parameter space and to constrain key physical properties, including stellar mass, SFR, dust attenuation, and mass-weighted age. The resulting posterior distributions were used for further interpretation in Section 4.

3.2.2 Radio-based Star Formation Rate Estimation

Star-forming galaxies emit both thermal (free-free) and non-thermal (synchrotron) radiation in the radio regime. Their total radio spectra are typically modelled as the superposition of two power-law components:

$$S_{\text{tot}}(\nu) = S_{\text{th}}(\nu_0) \left(\frac{\nu}{\nu_0} \right)^{-0.1} + S_{\text{nth}}(\nu_0) \left(\frac{\nu}{\nu_0} \right)^{-\alpha_{\text{nth}}}, \quad (2)$$

where S_{th} and S_{nth} are the thermal and non-thermal components at a reference frequency ν_0 , and α_{nth} is the non-thermal synchrotron spectral index. For frequencies below a few GHz, the synchrotron component dominates, especially at ~ 150 MHz.

Assuming that the observed radio emission arises primarily from star formation processes, we estimated the SFRs using the empirical relation $L_{150} = L_1 \psi^\beta$ derived by Gürkan et al. (2018), where L_{150} is the rest-frame 150 MHz monochromatic luminosity in W Hz^{-1} , ψ is the SFR in $M_\odot \text{ yr}^{-1}$. We adopted their best-fit parameters from Smith et al. (2021): $\log_{10} L_{150\text{MHz}} = (22.221 \pm 0.008) + (1.058 \pm 0.007) \log_{10}(\psi / M_\odot \text{ yr}^{-1})$.

The estimation of the star-formation rate from radio emission can also be affected by other factors, such as the stellar mass of the host galaxy (Gürkan et al. 2018). To improve the reliability of our estimates, we adopt a correlation that includes an explicit dependence on stellar mass, as presented by Smith et al. (2021): $\log_{10}(L_{150\text{MHz}} / \text{W Hz}^{-1}) = (0.90 \pm 0.01) \log_{10}(\psi / M_\odot \text{ yr}^{-1}) + (0.33 \pm 0.04) \log_{10}(M / 10^{10} M_\odot) + 22.22 \pm 0.02$. In our case, no archival stellar mass measurements are available for any of the three candidates. We therefore used the stellar masses estimated from our SED fitting in this relation and compared the resulting SFRs with those derived from the pure radio-flux relation. As the SED-based stellar mass estimates partly rely on optical data, they may also introduce some bias. For comparison, the resulting SFRs are listed in Table 2, where the SFRs derived from the radio-flux-only relation are denoted as $\text{SFR}_{\text{radio}}$, and those obtained using the mass-dependent relation are denoted as $\text{SFR}_{\text{radio w.m.}}$.

Monochromatic luminosities at rest-frame 150 MHz were derived by first extrapolating the observed LoTSS 144 MHz flux densities to 150 MHz using a standard synchrotron spectral slope ($\alpha_{\text{nth}} = -0.7$), following $S_{150} = S_{144} (150/144)^{\alpha_{\text{nth}}}$ applying a full k-correction. These extrapolated fluxes were combined with redshift estimates, using spectroscopic values where available and best-fit photometric (SED) redshifts otherwise, to compute L_{150} .

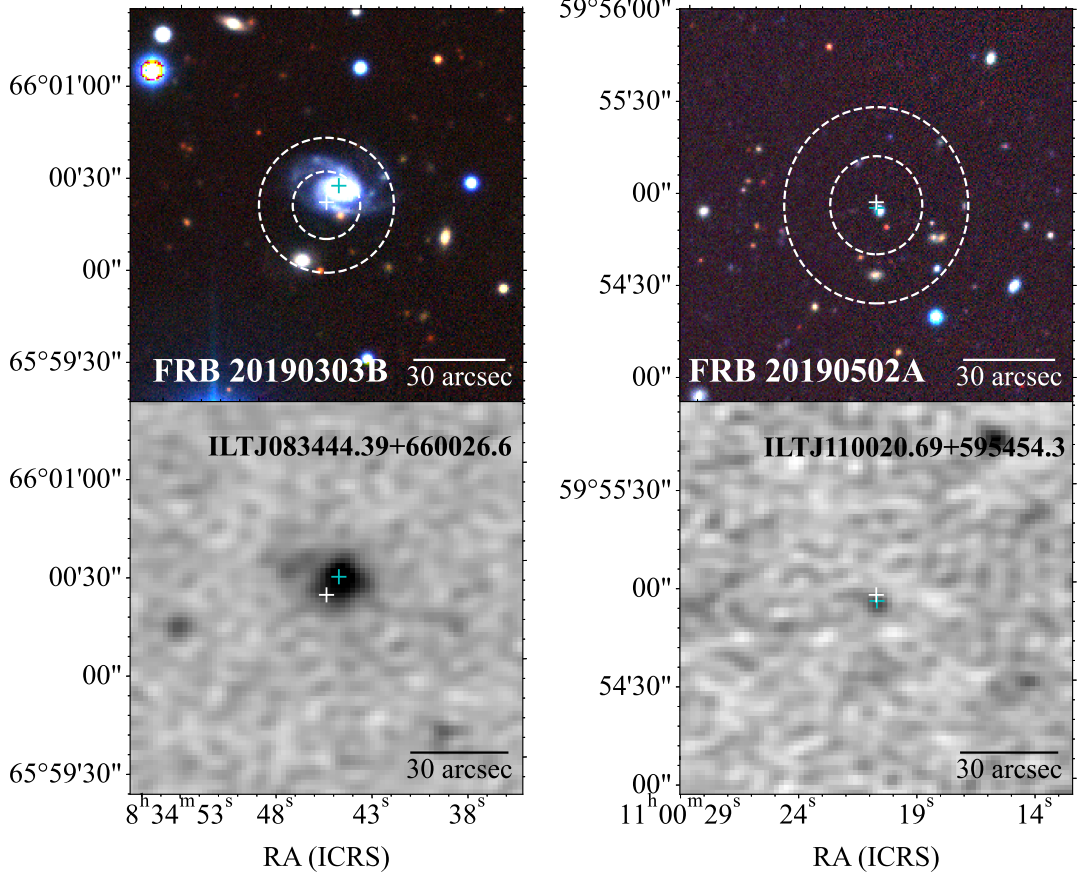


Figure 3. Optical and radio images of two secure candidates. *Top panels*: False-colour RGB images constructed from the g , r , and z bands of the Dark Energy Spectroscopic Instrument (DESI) Legacy Imaging Surveys for two secure candidates. The white ellipses represent the 1σ and 2σ localisation uncertainty regions of the FRB, with the white cross marking the FRB centroid and the cyan cross indicating the position of the matched LoTSS radio source. *Bottom panels*: LoTSS DR2 radio continuum images of the same regions.

3.2.3 $H\alpha$ -derived Star Formation Rate

For sources with optical spectra showing $H\alpha$ emission, SFRs were estimated based on the extinction-corrected $H\alpha$ luminosity, following the calibration of Kennicutt (1998):

$$\text{SFR} [M_\odot \text{ yr}^{-1}] = 7.9 \times 10^{-42} L(H\alpha) [\text{erg s}^{-1}] \quad (3)$$

In cases where the $H\alpha$ emission line is blended with [NII], we assumed a fixed [NII] contamination fraction of 29 percent based on Faisst et al. (2018), and subtracted this contribution from the total blended flux.

Galactic extinction corrections were applied using the extinction curve of Cardelli et al. (1989) with $R_V = 3.1$, and colour excess $E(B-V)$ values were obtained from the SFD dust map (Schlegel et al. 1998). The attenuation at the wavelength of $H\alpha$ was computed as $A(H\alpha) = 2.6 E(B-V)$ (Kennicutt et al. 2008).

For sources without detected $H\beta$ emission, internal attenuation was estimated using the best-fit A_V for young stellar populations obtained from CIGALE SED fitting. Following Calzetti et al. (2000), gas attenuation was calculated as $A_V^{\text{gas}} = 1.7 A_V^{\text{stars}}$, and converted to $H\alpha$ attenuation via $A(H\alpha) = 0.81 A_V^{\text{gas}}$.

In cases where both $H\alpha$ and $H\beta$ are detected, the internal extinction was derived from the Balmer decrement. Assuming Case B recombination with an intrinsic flux ratio of $H\alpha/H\beta = 2.86$ (Baker & Menzel 1938), the colour excess was calculated as:

$$E(B-V) = 1.97 \log_{10} \left(\frac{(H\alpha/H\beta)_{\text{obs}}}{2.86} \right). \quad (4)$$

The corrected $H\alpha$ luminosities were then used to derive SFRs using Equation 3.

4 RESULTS

4.1 Candidate Host Galaxies

4.1.1 Host galaxy of FRB 20190303B

FRB 20190303B has a CHIME position centred at R.A., Dec. = $128.6877, +66.0059$, with a 1σ localisation uncertainty of 11 arcseconds. A spatially consistent radio source, ILTJ083444.39+660026.6, is detected in the LoTSS catalogue at R.A., Dec. = $128.6850, +66.0074$, with a separation of 6.7 arcseconds and an integrated flux density of 5.493 mJy at 144 MHz. The radio emission appears to be extended, with significant flux detected both in the compact central region and along one of the spiral arms of the galaxy, coincident with the FRB localisation. As shown in Fig. 3, this spatial alignment suggests ongoing star formation activity near the FRB site.

The candidate host galaxy, MCG+11-11-014, is clearly resolved in the Dark Energy Camera Plane Survey (DECaPS; Schlafly et al.

Table 1. Basic properties of the CHIME/FRB events and their matched LoTSS DR2 radio counterparts. Dispersion measures (DMs) and the corresponding Galactic contributions at the FRB positions are taken from the CHIME/FRB baseband catalogue (CHIME/FRB Collaboration et al. 2024). The extragalactic DM values, corrected for the Milky Way contribution using the NE2001 model (Cordes & Lazio 2002), are adopted from CHIME/FRB Collaboration et al. (2021). The table reports four redshift estimates: z_{FRB} , inferred from the central DM–redshift relation of Macquart et al. (2020) (see their Fig. 2) following the method described in Section 3.1, with uncertainties derived from the intrinsic scatter (central 90 percent range) of the relation; z_{spec} , the spectroscopic redshift from the DESI Extragalactic Science Project and from this work, respectively; z_{phot} , the photometric redshift of the associated host galaxy from Zhou et al. (2021); and $z_{\text{DM Tang23}}$, the DM–redshift estimate reported by Tang et al. (2023). The positions and flux densities of the LoTSS counterparts are taken from Shimwell et al. (2022).

FRB Name	FRB 20190303B	FRB 20190502A	FRB 20181214C
LoTSS ID	ILTJ083444.39+660026.6	ILTJ110020.69+595454.3	ILTJ114334.93+600331.4
Optical ID	SDSS J083444.42+660026.5 (MCG+11-11-014)	SDSS J110020.55+595454.4	SDSS J114335.11+600334.9
RA _{FRB} (deg)	128.6877	165.0863	175.8997
Dec _{FRB} (deg)	66.0059	59.9156	60.0573
DM (pc cm ⁻³)	193.4292	625.738	632.8323
DM _{MW} (pc cm ⁻³)	41	44	41
DM _{exc,MW} (pc cm ⁻³)	146.4	590.8	599.5
z_{FRB}	$0.1030^{+0.0364}_{-0.0405}$	$0.4933^{+0.1741}_{-0.1941}$	$0.5416^{+0.1912}_{-0.1583}$
z_{spec}	0.0656 ± 0.0026	0.2803 ± 0.0100	–
z_{phot}	0.063 ± 0.011	0.274 ± 0.034	0.447 ± 0.261
$z_{\text{DM Tang23}}$	–	$0.606^{+0.150}_{-0.321}$	$0.616^{+0.152}_{-0.332}$
RA _{LoTSS} (deg)	128.6850	165.0862	175.8955
Dec _{LoTSS} (deg)	66.0074	59.9151	60.0587
Flux (mJy)	5.49 ± 0.41	0.33 ± 0.14	$1.51 \pm 0.37^{\dagger}$
Separation _{FRB-LoTSS} (arcsec)	6.7	1.9	9.1
Classification	Secure	Secure	<i>Tentative</i>

[†] Flux derived in this work owing to the extended nature of the source and the low signal-to-noise ratio of the peak; the corresponding LoTSS DR2 catalogue value is 4.58 ± 0.91 mJy.

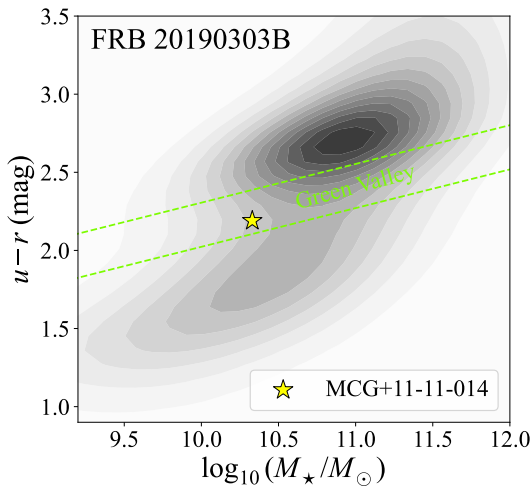


Figure 4. Colour–mass diagram, where green-valley galaxies lie between the two green lines. The yellow star marks the FRB 20190303B host-galaxy candidate MCG+11-11-014. Contours indicate the SDSS spectroscopic sample (Chang et al. 2015). Green lines show the green valley defined by Schawinski et al. (2014).

2018) optical images as a moderately inclined spiral galaxy, exhibiting a bright, reddened central core and loosely wound outer spiral arms. Its global $g - r$ colour is 0.66 mag. To better quantify the physical properties implied by this colour, we further used the integrated optical colours and photometric measurements from SDSS, which

provides the u -band that is unavailable in DECaPS. Its rest-frame $u - r = 2.08$ mag (from SDSS) places it firmly within the ‘green-valley’ regime of the optical colour–mass diagram shown in Fig. 4, according to the definition of Schawinski et al. (2014). Such green-valley systems are commonly associated with galaxies transitioning from active star formation to quiescence.

To assess the galaxy morphology and colour gradient, we performed non-parametric elliptical isophotal fitting using the Photutils package (Bradley 2023). The fitting was carried out iteratively to determine stable geometric parameters of the galaxy. The ellipticity and inclination were first estimated from multiple fits and then fixed at their best-fitting values ($\epsilon = 0.34 \pm 0.05$, $i = 49 \pm 4^\circ$) to minimise degeneracies and ensure consistent radial sampling. Using these fixed geometric parameters, identical sets of elliptical isophotes were applied to both the g - and r -band images, allowing surface brightness profiles and colours to be measured at matched isophotal radii. The resulting g - and r -band surface brightness profiles, along with the radial $g - r$ colour profile, are shown in Fig. 5. The colour profile reveals a reddened bulge, with $\mu_g - \mu_r$ reaching ~ 1.5 mag in the inner region and declining to below ~ 0.5 mag in the outer disk. The inferred inclination is consistent with the typical morphologies of FRB host galaxies reported by Bhardwaj et al. (2024a).

We additionally performed SED fitting using multi-band photometry from GALEX (FUV, NUV), SDSS (u, g, r, i, z) (Ahumada et al. 2020), 2MASS (J, H, K_s), WISE (W1–W4) (Cutri et al. 2013), and Herschel/SPIRE (PMW, PSW). The best-fit stellar population model yields a stellar mass of $\log_{10} M_{\star, \text{SED}} [\text{M}_\odot] = 10.33 \pm 0.06$ and a star formation rate of $\log_{10} \text{SFR}_{\text{SED}} [\text{M}_\odot \text{ yr}^{-1}] = 0.52 \pm 0.09$. The host’s WISE mid-infrared colours also place it in the star-forming

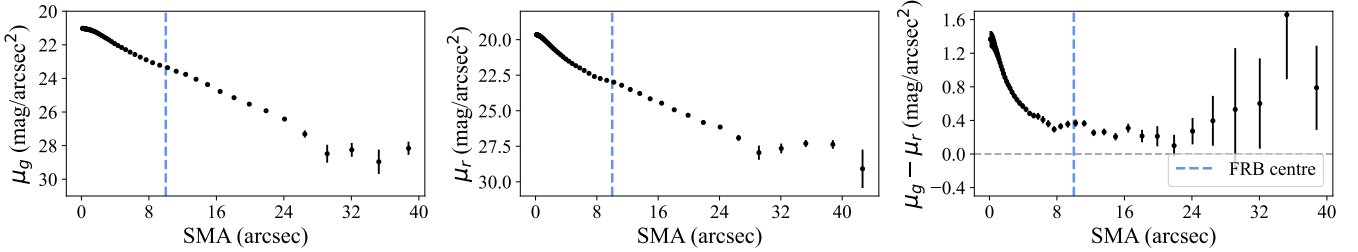


Figure 5. Radial surface brightness profiles of the candidate FRB 20190303B host galaxy MCG+11-11-014 in the g -band (left), r -band (middle), and the corresponding colour profile ($\mu_g - \mu_r$, right). Error bars represent photometric uncertainties propagated from the intensity measurements. The vertical dashed lines indicate the semi-major axis (SMA) radius corresponding to the FRB centre position. The colour profile shows a mild radial gradient, potentially reflecting variations in stellar population or internal dust attenuation.

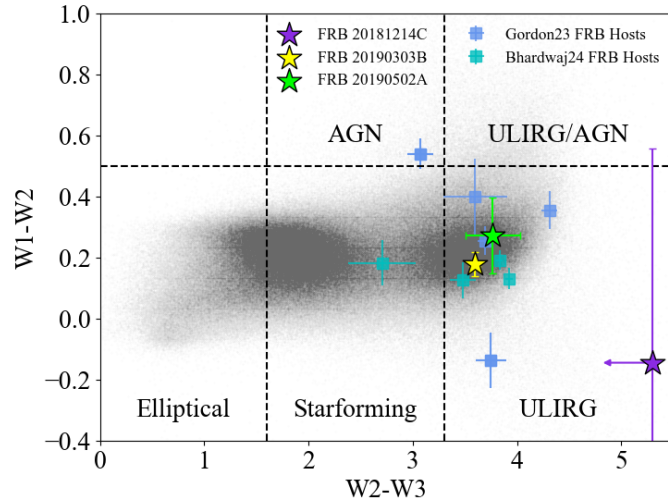


Figure 6. The $W_2 - W_3$ versus $W_1 - W_2$ diagram, where W_1 , W_2 , and W_3 denote the WISE mid-infrared photometric bands, used to separate objects into different classes. The purple, yellow, and green stars indicate the host galaxies selected in this work and listed in Table 1. The arrow marks an upper limit for FRB 20181214C, as no W_3 measurement is available. The background black dots are SDSS spectroscopic galaxy sample (Chang et al. 2015). The blue square indicates the FRB hosts in Gordon et al. (2023), and the cyan square indicates the FRB hosts in Bhardwaj et al. (2024b).

galaxy region, as defined by the WISE colour criteria described in Section 4.2 (Fig. 6), supporting its classification as a dust-rich, star-forming spiral.

We obtained an optical spectrum of the galaxy’s central region using the SPectrograph for the Rapid Acquisition of Transients (SPRAT) instrument on the Liverpool Telescope, as part of project ID:PL24B06 (PI: R.A.J. Eyles-Ferris), with a total integration time of 2400 seconds. The wavelength coverage was $3711.36 - 8202.12$ Å, and the spectral resolution was 18 Å. From this spectrum, we derive a spectroscopic redshift of $z = 0.0656 \pm 0.0026$. The fitting result is shown in Fig. B1.

The $H\alpha$ and $[\mathrm{N}\,\mathrm{II}]$ lines in the optical spectrum of MCG+11-11-014 are not well resolved owing to the limited spectral resolution. We therefore estimated the $H\alpha$ flux following the method described in Section 3.2.3. From the stellar attenuation derived via SED fitting, we obtained an internal dust attenuation of $A_V = 0.6$ mag, corresponding to a gas-phase attenuation of $A(H\alpha) = 0.83$ mag.

After applying these corrections, the extinction-corrected $H\alpha$ luminosity yields a star formation rate of $\log_{10} \mathrm{SFR}_{H\alpha} [\mathrm{M}_\odot \mathrm{yr}^{-1}] = -0.84 \pm 0.07$. This value is significantly lower than the SED-derived SFR (see Table 2), likely due to uncertainties in spectral flux calibration and line deblending, or to the slit capturing only the galaxy’s central region along with a small portion of its outer disk. Given these limitations, the SED-derived SFR is likely to provide a more representative estimate of the galaxy’s global star-forming activity. The discrepancy between the SFRs inferred from $H\alpha$ emission and SED fitting will be further discussed in Section 4.2.

To assess redshift consistency, we compared this spectroscopic measurement with redshifts estimated from FRB dispersion measures. Using the Macquart relation (Macquart et al. 2020), and following the method in Section 3.1, the inferred redshift for FRB 20190303B is $z = 0.1030^{+0.0364}_{-0.0405}$, based on a total DM of $193.4292 \mathrm{pc\,cm}^{-3}$ and Galactic contribution $\mathrm{DM}_{\mathrm{MW}} = 41 \mathrm{pc\,cm}^{-3}$, as listed in Table 1. The spectroscopic redshift is somewhat lower than the DM-based estimate, but within $1-2\sigma$ of the confidence interval. For completeness, we also note that the host galaxy has a photometric redshift of $z_{\mathrm{phot}} = 0.063 \pm 0.011$ from DESI DR8 (Duncan 2022), which is broadly consistent with both the spectroscopic and DM-inferred redshifts within the uncertainties. Additionally, we searched for radio detections at other frequencies and found no counterparts in the NRAO VLA Sky Survey (NVSS; Condon et al. 1998; 1.4 GHz) or the Faint Images of the Radio Sky at Twenty-one centimeters (FIRST; Becker et al. 1995; 1.5 GHz).

Taken together, the small FRB-radio separation, alignment with the spiral arm, redshift consistency across DM, photometric, and spectroscopic methods, and multi-wavelength indications of active star formation, all support a robust association. We therefore propose FRB 20190303B and MCG+11-11-014 as a likely FRB-host association.

4.1.2 Host galaxy of FRB 20190502A

FRB 20190502A was detected by CHIME at R.A., Dec. = $165.0818, +59.9146$ with a localisation uncertainty of $15'' \times 16''$ (1σ). The nearest radio source in the LoTSS catalogue is ILTJ110019.68+595455.5 at R.A., Dec. = $165.0862, +59.9151$, located just $1.87''$ away, with an integrated flux density of $0.3337 \mathrm{mJy}$ at 144 MHz, making it a strong positional match. The putative host galaxy, WISEA J110020.52+595454.2, is detected in the DESI Extragalactic Science Project² and has an available optical spectrum

² <https://data.desi.lbl.gov/doc/releases/dr1/>

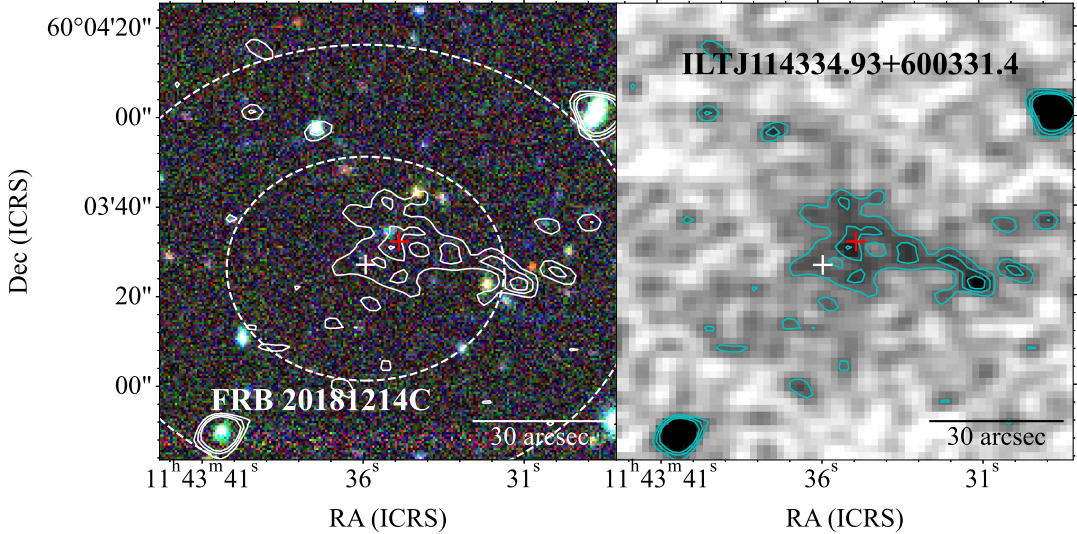


Figure 7. Optical and radio images of the tentative candidate. *Left panel:* False-colour RGB images constructed from the g , r , and z bands of the DESI Legacy Imaging Surveys for the tentative candidate. The white ellipses represent the 1σ and 2σ localisation uncertainty regions of the FRB, with the white cross marking the FRB centroid and the red cross indicating the position of the matched LoTSS radio source. *Right panel:* LoTSS DR2 radio continuum images of the same regions. Cyan contours represent emission levels at 2, 3, and 4 times the local RMS noise.

(target ID: 39633386943283235). No radio counterparts at higher frequencies are detected.

From the DESI spectrum we identify several prominent emission lines, yielding a best-fit spectroscopic redshift of $z = 0.2803 \pm 0.0100$. Although this is formally lower than the central Macquart relation estimate of $0.4933^{+0.1741}_{-0.1941}$, it remains statistically consistent once the large intrinsic scatter of the relation is considered. To further account for uncertainties in the host and IGM contributions, we adopt the Bayesian DM– z estimate reported by Tang et al. (2023), which assumes log-normal priors on DM_{host} . Their quoted value of $z = 0.606^{+0.150}_{-0.321}$ is marginally consistent with both the Macquart relation-based and spectroscopic estimates, lending support to a physical association between the FRB and this galaxy. Among the overlapping FRB sample, approximately 80 percent of Macquart-derived redshifts lie below $z \sim 0.8$, and two of our candidates are consistent with this dominant redshift range.

The host candidate exhibits moderately red optical colours, with $g - r \approx 0.92$, which might suggest a passive or quiescent galaxy. However, its infrared properties indicate otherwise. The WISE mid-infrared colour $W2 - W3 \approx 3.77$ points to a substantial infrared excess, consistent with active star formation. This discrepancy suggests the galaxy is a dusty star-forming system, where the red optical colours are likely due to internal dust attenuation rather than a lack of recent star formation.

The optical spectrum of WISEA J110020.52+595454.2 from the DESI Extragalactic Sources Project includes several well-detected emission lines. Following the procedure described in Section 3.2.3, we corrected for Galactic extinction and derived the internal dust attenuation using the Balmer decrement, based on the observed $\text{H}\alpha/\text{H}\beta$ flux ratio. Assuming Case B recombination, we calculated a colour excess of $E(B-V) = 0.091$ mag. The extinction-corrected $\text{H}\alpha$ luminosity yields a star formation rate of $\log_{10} \text{SFR}_{\text{H}\alpha} [\text{M}_\odot \text{yr}^{-1}] = -0.06 \pm 0.04$, using the calibration from Kennicutt (1998). This value is substantially below the SFR inferred from the CIGALE modelling. A detailed discussion of the discrepancy between the SFRs inferred from $\text{H}\alpha$ emission and SED fitting is presented in Section 4.2.

4.1.3 Tentative host galaxy of FRB 20181214C

FRB 20181214C is centred at R.A., Dec. = $175.8997, +60.0573$, with a 1σ localisation uncertainty of $31''$ in right ascension and $25''$ in declination, according to the CHIME/FRB baseband catalogue. A corresponding radio source is detected in the LoTSS DR2 catalogue as ILTJ114334.93+600331.4 at R.A., Dec. = $175.8955, +60.0587$ with a total flux of 4.575 mJy and a peak signal-to-noise ratio of 2.73. The source appears extended, with a deconvolved major axis of $33''$ and minor axis of $28''$.

We identified an optical counterpart to the LoTSS source in the DESI imaging survey. The counterpart is extremely blue, with magnitudes of $g = 22.59$, $r = 22.04$, and $z = 21.96$, and has no spectroscopic measurement available. Zhou et al. (2021) report a photometric redshift of $z = 0.447 \pm 0.261$, broadly consistent with other estimates in the literature, including 0.223 ± 0.121 (Ahumada et al. 2020) and 0.341 ± 0.157 (Duncan 2022). The redshift inferred from the Macquart relation for FRB 20181214C is $z = 0.5416^{+0.1912}_{-0.1583}$, while Tang et al. (2023) reported $z = 0.616^{+0.152}_{-0.332}$. All of these estimates are consistent within uncertainties, supporting the plausibility of an association between the FRB and this galaxy.

Assuming a redshift of ~ 0.447 , the corresponding projected physical size of the radio emission is approximately 190×161 kpc, suggesting an extended source, possibly a star-forming galaxy with large-scale radio emission. Due to the very faint and extended nature of the radio source, as seen in the right panel of Fig. 7, we remeasured its integrated flux density using a custom aperture. Specifically, we defined an elliptical aperture centred at R.A. = $11^{\text{h}}43^{\text{m}}35.05^{\text{s}}$, Dec. = $+60^{\circ}03'31.14''$, with semi-major and semi-minor axes of $15''$ and $10''$, respectively. This aperture was chosen to enclose the emission within the 2σ contour. The resulting integrated flux density is measured to be 1.51 mJy.

To estimate the uncertainty on the integrated flux density, we consider two primary sources of error: the background noise and the absolute flux calibration uncertainty. The total uncertainty is given by $\sigma_{\text{total}} = \sqrt{(\sigma_{\text{rms}} \cdot \sqrt{N_{\text{beam}}})^2 + (f_{\text{cal}} \cdot S_{\text{int}})^2}$, where σ_{rms} is the local background noise measured from the image in units

Table 2. Stellar mass and star formation rates derived from different methods

FRB Name	FRB 20190303B	FRB 20190502A	FRB 20181214C
$\log_{10} \text{SFR}_{\text{SED}} [\text{M}_\odot \text{ yr}^{-1}]$	0.52 ± 0.09	0.61 ± 0.12	0.31 ± 0.36
$\log_{10} \text{SFR}_{\text{radio}} [\text{M}_\odot \text{ yr}^{-1}]$	$0.51^{+0.05}_{-0.05}$	$0.64^{+0.15}_{-0.23}$	$1.67^{+0.46}_{-0.80}$
$\log_{10} \text{SFR}_{\text{radio w m}} [\text{M}_\odot \text{ yr}^{-1}]$	$0.48^{+0.06}_{-0.07}$	$0.47^{+0.18}_{-0.27}$	$2.16^{+0.54}_{-0.94}$
$\log_{10} \text{SFR}_{\text{H}\alpha} [\text{M}_\odot \text{ yr}^{-1}]$	-0.84 ± 0.07	-0.06 ± 0.04	-
$\log_{10} M_{\star, \text{SED}} [\text{M}_\odot]$	10.33 ± 0.06	10.77 ± 0.07	9.45 ± 0.23

of mJy/beam, S_{int} is the measured integrated flux density, and f_{cal} is the assumed fractional calibration uncertainty. The number of synthesized beams within the measurement aperture is computed as $N_{\text{beam}} = A_{\text{aperture}}/A_{\text{beam}}$, with the beam area given by $A_{\text{beam}} = 1.1331 \times \theta_{\text{maj}} \times \theta_{\text{min}}$, where θ_{maj} and θ_{min} are the full width at half maximum (FWHM) of the synthesized beam in arcseconds. In our case, the aperture corresponds to an ellipse with a major axis of $15''$ and a minor axis of $10''$, and the beam size is $6'' \times 6''$. A conservative 20 percent calibration uncertainty ($f_{\text{cal}} = 0.20$) is adopted following the LoTSS DR2 recommendations (Shimwell et al. 2022). The total uncertainty on the measured flux density is estimated to be 0.372 mJy. Considering the updated flux estimate, the source now falls within the 99.9 percent contour in Fig. 2, indicating a lower likelihood of being intrinsically associated with the FRB.

The infrared counterpart is detected in WISE, while no X-ray emission is detected at the corresponding position in existing X-ray catalogues (e.g. 4XMM-DR13; Webb et al. 2020, and the 2SXPS Swift catalogue; Evans et al. 2020). In addition, the WISE colour diagram also argues against the presence of a bright active galactic nucleus (AGN). No radio counterparts at higher frequencies are detected, combined with the LoTSS detection, implies a steep radio spectral index, consistent with star formation as the dominant emission mechanism. Given the radio morphology, blue optical colours, the lack of AGN signatures and the photometric redshift consistent with the FRB DM-based distance estimate, we include this source as a tentative candidate host for FRB 20181214C. However, we cannot rule out the possibility that part of the emission arises from jet-related activity associated with a nearby AGN. In this scenario, any star formation inferred from the radio emission may be affected by jet-ISM interactions, and we therefore treat this source with caution.

We additionally performed SED fitting using multi-band photometry from SDSS (u, g, r, i, z) and WISE (W1–W2). The best-fit stellar population model yields a stellar mass of $\log_{10} M_{\star, \text{SED}} [\text{M}_\odot] = 9.45 \pm 0.23$ and a star formation rate of $\log_{10} \text{SFR}_{\text{SED}} [\text{M}_\odot \text{ yr}^{-1}] = 0.31 \pm 0.36$. The redshift corresponding to the best-fitting model is 0.27.

4.2 Comparison with Previously Identified FRB Host Galaxies

We analysed the infrared (IR) colour properties of our candidate host galaxies using data from the Wide-field Infrared Survey Explorer (WISE). Each candidate was cross-matched to the nearest counterpart in the AllWISE catalogue³, and we manually inspected the corresponding optical images (from DESI and SDSS) to confirm that the infrared emission originated from the correct host candidate, avoiding contamination from nearby sources.

To classify the galaxies, we adopted colour-based criteria similar to those proposed by Mingo et al. (2016, 2019). These diagnostics

exploit the distinct infrared behaviours of different galaxy populations: AGN-dominated systems, luminous infrared galaxies (LIRGs), ultraluminous infrared galaxies (ULIRGs), and normal star-forming or quiescent galaxies occupy different regions in the WISE W1–W2 versus W2–W3 colour space, reflecting variations in dust heating, star-formation activity, and nuclear emission. The measured WISE magnitudes (W1, W2, W3) of the candidate hosts are listed in Table A1, A2 and A3, whereas the colour–colour diagram is shown in Fig. 6.

We also included in Fig. 6 the WISE colours of FRB host galaxies previously analysed by Gordon et al. (2023) and Bhardwaj et al. (2024b) for comparison. According to our adopted classification scheme, two of our candidate hosts with reliable WISE detections fall in the region of the diagram typically occupied by dust-rich, infrared-luminous galaxies. These candidates also exhibit WISE colours consistent with those of previously confirmed FRB host galaxies, suggesting similar dusty star-forming environments. The WISE colour analysis provides complementary evidence for the active, possibly dust-obscured nature of the host galaxies, particularly where optical indicators (e.g. SFR from H α) may be affected by internal extinction.

We further compared the star formation rates and stellar masses of our candidate host galaxies with the FRB host samples presented by Heintz et al. (2020); Gordon et al. (2023); Loudas et al. (2025). The star formation rates derived through multiple methods from this work, including spectral energy distribution (SED) fitting, H α emission, and radio luminosity – do not show significant deviations from the distributions of previously identified FRB host galaxies. For clarity, the Gordon et al. (2023) sample is shown in both Fig. 6 and Fig. 8 for comparison. Some hosts lack WISE photometry and are therefore excluded from Fig. 6, while an additional redshift cut is applied in Fig. 8, leading to different sample sizes.

According to the SED fitting results, all three candidates lie on the star-forming main sequence, suggesting they are actively forming stars. However, as shown in Fig. 8, we find that the SFRs derived from H α fluxes are significantly lower than those inferred from SED modelling, particularly for FRB 20190303B and FRB 20190502A. This discrepancy can be understood in terms of the different physical timescales and sensitivities probed by the two indicators: H α emission traces very recent star formation on timescales of $\lesssim 10$ Myr, whereas SED-based SFRs reflect an average over longer timescales of ~ 100 Myr and are therefore less sensitive to short-term variability. In addition, both of these galaxies exhibit signs of internal dust attenuation: they have compact optical morphologies and reddened central regions. Specifically, the inner core of the spiral galaxy MCG+11-11-014 (associated with FRB 20190303B) displays substantially redder colours, while the host of FRB 20190502A also shows a compact, dusty profile. These features suggest that dust obscuration may play an important role, potentially leading to an underestimation of the H α -derived SFRs.

Several statistical studies in the nearby universe have directly compared star formation rates from H α emission to those from SED fitting. Salim et al. (2007) report that the UV/SED-based SFRs

³ <https://wise2.ipac.caltech.edu/docs/release/allwise/>

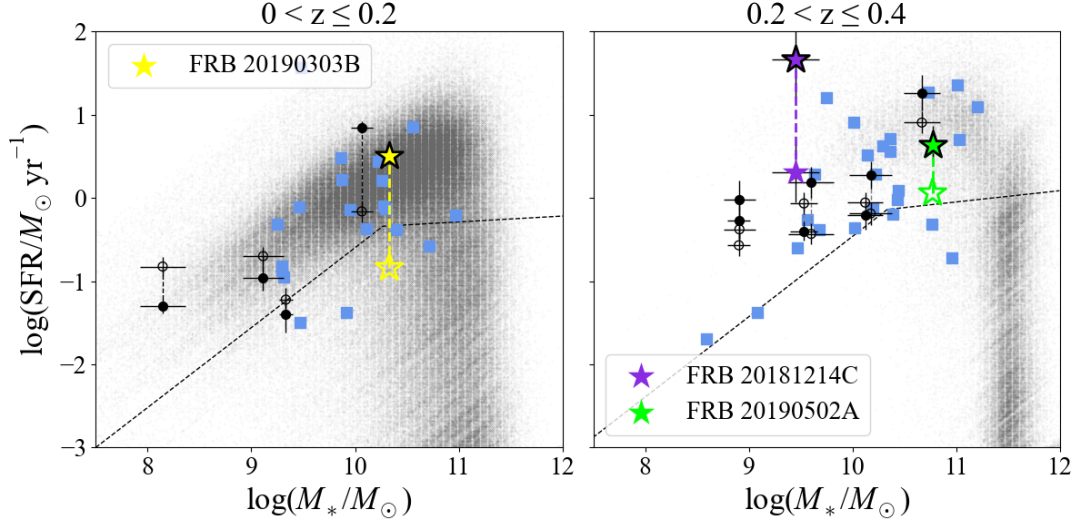


Figure 8. Stellar mass versus star-formation rate for the host galaxy candidates in two redshift bins. Filled stars indicate SFRs derived from SED fitting, while hollow stars represent those derived from $H\alpha$ fluxes. Purple, yellow, and green stars correspond to FRB 20190303B, FRB 20190502A, and FRB 20181214C, respectively. Stars with black outlines indicate the SFRs inferred from low-frequency radio emission. For both FRB 20190303B and FRB 20190502A, the radio-inferred SFRs overlap on the SED-derived values, indicating consistency between these two tracers. The background consists of the SDSS spectroscopic galaxy sample (Chang et al. 2015), while blue squares denote the sample from Loudas et al. (2025). Solid black circles represent the SED-derived SFRs from Gordon et al. (2023), and hollow circles represent the $H\alpha$ -derived SFRs from Heintz et al. (2020). The dashed line indicates the division between star-forming and quiescent galaxies.

‘compare remarkably well’ with SFRs from SDSS $H\alpha$ measurements, with any deviations mainly due to differing dust-extinction corrections. Catalán-Torrecilla et al. (2015) (Calar Alto Legacy Integral Field Area, CALIFA survey) further showed that with integral field spectroscopy one can robustly correct $H\alpha$ for dust and achieve good agreement with hybrid tracers ($H\alpha$ + IR or UV + IR) across a wide SFR range ($0.03\text{--}20 M_\odot \text{yr}^{-1}$). Local studies demonstrate a good calibration between $H\alpha$ and SED-derived SFRs, and highlight the importance of applying consistent dust attenuation corrections in both methods to avoid systematic offsets.

$H\alpha$ traces star formation over timescales of approximately 0 to 3–10 Myr, but its reliability is affected by two major systematic uncertainties: dust attenuation and sensitivity to the upper end of the initial mass function (IMF), especially in regions with intrinsically low star formation rates (Kennicutt & Evans 2012). In regions with moderate extinction, Balmer decrements (the flux ratio of recombination lines such as $H\alpha$ and $H\beta$) can be used to estimate and correct for attenuation (Kewley et al. 2002; Brinchmann et al. 2004; Moustakas et al. 2006). However, this method breaks down in circumnuclear starbursts or other dusty galaxies (e.g., Moustakas et al. 2006).

To investigate potential differences, we compared the SED-derived and $H\alpha$ -derived SFRs reported in Gordon et al. (2023) and Heintz et al. (2020), respectively. The comparison is shown in Fig. 8, where solid black circles indicate the SED-based SFRs, and hollow circles represent the $H\alpha$ -based values. In some cases, the SED-derived SFRs are significantly higher than those from $H\alpha$, although the majority of sources show good agreement between the two methods. However, due to the limited sample size, no statistically significant conclusion can be drawn for the host sample.

This discrepancy reinforces the importance of multi-wavelength SFR indicators when assessing the nature of FRB host galaxies, particularly in dusty or edge-on systems where optical tracers alone may be insufficient. As shown in Fig. 9, a portion of the known FRB host galaxies could potentially be detected by the LOFAR survey,

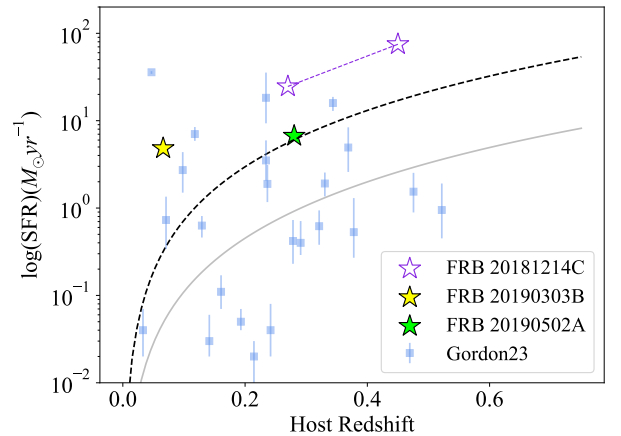


Figure 9. The required SFR to reach 0.30 mJy at 150 MHz for a given redshift (black dashed-line). The SFRs for other FRB hosts are taken from Gordon et al. (2023). Filled stars indicate FRBs with spectroscopic redshift measurements of their candidate hosts; hollow stars represent candidates with only photometric redshift estimates; in cases of large uncertainty (i.e. FRB 20181214C), two points are shown to indicate the lower and upper limits for the same host galaxy. The grey solid line indicates the sensitivity limit achieved in the LOFAR Deep Fields.

provided that the relevant regions of the sky are covered. Currently, none of the hosts reported in Gordon et al. (2023) fall within the LOFAR footprint. However, with the ongoing progress of the LoTSS survey, we anticipate identifying more FRB host candidates at low radio frequencies.

5 DISCUSSION

Our pilot study demonstrates the feasibility of identifying FRB host galaxy candidates using low-frequency radio continuum emission alone, offering a complementary approach to traditional optical association techniques. This method holds particular promise for uncovering dusty or optically faint host galaxies that may otherwise be missed. However, several limitations must be considered when interpreting these results.

First, the sample remains limited, with only two secure and one tentative host associations. This is due to the modest overlap between the CHIME/FRB baseband-localised catalogue and the current LoTSS DR2 footprint, as well as the still-small size of the CHIME/FRB baseband dataset and the depth limitations of the LOFAR survey. As such, our findings should be regarded as exploratory. Nevertheless, the successful identification of host candidates via radio emission highlights the potential of future large-scale, radio-selected FRB host samples. The forthcoming LOFAR 2.0 upgrade is expected to substantially enhance this potential. By enabling full-array operations, increased bandwidth, and stable, automated calibration pipelines, LOFAR 2.0 will facilitate commensal observations and broader sky coverage. In addition, the increased use of international stations will deliver subarcsecond astrometric precision, further reducing the probability of false positive associations in our cross-matching procedure. Although no specific RMS sensitivity targets have been quoted, the system is expected to approach the thermal-noise limit under a wider range of observing conditions (LOFAR2.0 Science Working Group 2023). Deep fields in LoTSS DR1 have already achieved 3σ detection limits of $40\text{--}60\,\mu\text{Jy beam}^{-1}$ in regions such as ELAIS-N1 and the NEP (Best et al. 2023). With comparable or improved sensitivity and extended overlap with future CHIME/FRB baseband releases, the number of detectable host candidates could increase significantly, potentially doubling based on the projected detection limits (see Fig. 9).

Looking further ahead, the Canadian Hydrogen Observatory and Radio-transient Detector (CHORD; Vanderlinde et al. 2019) will build on CHIME to provide a powerful next-generation facility for FRB studies. Operating over an ultra-wide 300–1500 MHz band, CHORD will be particularly sensitive to high-redshift FRBs, for which low-frequency observations maximise detectability and dispersion leverage. The inclusion of long-baseline outrigger stations will deliver arcsecond- to milliarcsecond-level localisations for large FRB samples, substantially reducing cross-matching uncertainties and enabling robust population-level studies of FRB host galaxies across cosmic time. In addition to CHORD, more immediate opportunities for improved FRB localisation and host identification are expected from the CHIME/FRB Outrigger system (CHIME/FRB Collaboration et al. 2025), which will provide arcsecond-level localisations for a growing sample of FRBs and enable the construction of new catalogues in the near future. In concert with the depth and improved astrometry from LOFAR 2.0, this will make radio-selected FRB host samples both much larger and far more secure.

Second, although radio selection avoids the optical biases that disfavour dusty or high-redshift galaxies, it introduces its own selection effects. LoTSS is primarily sensitive to synchrotron-emitting galaxies and is therefore biased toward actively star-forming systems with sufficient radio brightness. Quiescent or low-SFR hosts may fall below the detection threshold, reducing the completeness of the radio-selected sample. This limitation is particularly relevant given that several well-localised FRBs have been associated with low-SFR or even early-type galaxies (e.g. FRB 20180924B; Bannister et al. 2019, FRB 20190523; Ravi et al. 2019, FRB 20240209A; Eftekhari et al. 2025; Shah et al. 2025). Moreover, not all low-frequency ra-

dio emission necessarily traces star formation. Possible mechanisms for providing excess radio emission at low SFRs include pulsars, type Ia supernovae, residual contamination by active galactic nuclei (AGN), and varying magnetic field properties (Smith et al. 2021; Sudoh et al. 2021). Chime/FRB Collaboration et al. (2025) identified 21 new FRB host galaxies using the CHIME/FRB Outrigger KKO. Two of these candidates have radio counterparts in the LoTSS survey. FRB 20230926A is coincident with the extended 144 MHz source ILTJ75629.78+414836.4; however, the high probability of chance alignment disfavours a genuine association from a statistical perspective. In contrast, the repeating FRB 20231128A is associated with a luminous PRS detected in the FIRST survey, and a bright LoTSS counterpart (ILTJ131819.22+425958.9) is also found at the position of the FIRST source. The observed radio emission may arise either from a background AGN or from star-formation activity within the host galaxy. In our work, we mitigate these effects by combining radio data with independent multi-wavelength diagnostics. In particular, we use mid-infrared colour–colour information and available X-ray constraints to assess the presence of AGN activity independently of the radio emission. For nearby and spatially resolved galaxies, radio morphology provides an additional discriminator, allowing us to distinguish emission associated with the host galaxy from potential background AGN. While these approaches enable robust classification in most cases, we acknowledge that ambiguities remain for a small number of sources, which are therefore treated on a case-by-case basis in our analysis.

Within these limitations, the observed properties of our candidate hosts are consistent with the star-forming main sequence, in line with the hypothesis that at least some FRBs originate from young, short-lived progenitors such as magnetars formed via core-collapse supernovae (e.g. Bochenek et al. 2020; Zhang 2023). However, this alignment may in part reflect the selection biases of LoTSS. As such, the current sample does not preclude contributions from alternative progenitor channels associated with older stellar populations or dynamical formation mechanisms. Disentangling these possibilities will require larger and more diverse samples, systematic comparisons across different FRB populations (including both repeaters and non-repeaters), as well as high-resolution imaging and multi-wavelength diagnostics to establish the physical origin of the detected radio emission.

To our knowledge, this is the first host-galaxy search conducted at low radio frequencies, whereas most FRB host galaxies to date have been identified using optical galaxy surveys. Having identified our host candidates through radio-selection, we now consider the association likelihood that would have been assigned using an optical method. We employed the commonly used Probabilistic Association of Transients to their Hosts (PATH)⁴ package (Aggarwal et al. 2021), a Bayesian framework used for FRB host identification in optical. We constructed optical candidate lists using SDSS DR9 *g*-band magnitudes and Petrosian radii (Ahn et al. 2012). Each candidate was assigned a posterior probability based on its angular separation from the FRB, relative brightness, and assumed offset distribution. Using the default prior settings, our results show that in the optical *g* band, MCG+11-11-014 has a ~ 65 percent probability of being the true host of FRB 20190303B, while SDSS J110020.55+595454.4 has a ~ 45 percent probability of hosting FRB 20190502A. For FRB 20181214C, no optical counterpart attains a host probability above 30 percent. According to previous optical host-identification studies (Fong et al. 2021; Gordon et al. 2023), a secure host is typ-

⁴ <https://github.com/FRBs/astropath>

ically required to have a chance-alignment probability of less than 10 percent, corresponding to a > 90 percent probability of being the true host. The host galaxies selected in this work are more difficult to identify using optical-based methods, highlighting the need for larger samples of radio-selected host candidates to enable a robust comparison between radio and optical selection approaches.

Among our candidate hosts, we observe apparent discrepancies between different SFR indicators. In all three cases, the $\text{H}\alpha$ -derived SFRs are systematically lower than those inferred from SED fitting or radio luminosity. While the small sample size precludes any general conclusion, these differences are plausibly attributable to a combination of internal dust attenuation and observational limitations, such as aperture effects or limited spectral resolution in the optical data. Similar discrepancies have been reported in other studies of dusty or compact galaxies (e.g. [Salim et al. 2007](#); [Kennicutt & Evans 2012](#)). FRB 20171020A also has a radio counterpart, detected between 2.1 and 16.7 GHz. Using the measured spectral index and the 1.4 GHz luminosity–SFR relation, the inferred star formation rate is $0.18^{+0.54}_{-0.17} \text{ M}_\odot \text{ yr}^{-1}$. In comparison, the SFR derived from SED fitting is $0.09 \pm 0.01 \text{ M}_\odot \text{ yr}^{-1}$ ([Lee-Waddell et al. 2023](#)). The slight discrepancy between the two estimates can be attributed to the large intrinsic scatter in the radio–SFR relation, which provides only an order-of-magnitude approximation. [Bhandari et al. \(2020\)](#) reported radio detections of FRB 20191001A at 5.5 and 7.5 GHz, and estimated a star formation rate of $\sim 11.2 \text{ M}_\odot \text{ yr}^{-1}$, which is comparable to the SFR of $8.06 \pm 2.42 \text{ M}_\odot \text{ yr}^{-1}$ reported from the dust-corrected $\text{H}\alpha$ line fluxes by [Heintz et al. \(2020\)](#). In recent work on the host galaxy of FRB 20201124A ([Dong et al. 2024](#)), VLA observations at 1.5–6 GHz revealed that the host has a radio-inferred SFR approximately 2.5 times higher than that inferred from $\text{H}\alpha$ luminosity. As shown in their fig. 6, which compares optical and radio SFRs, most FRB hosts have only upper limits on their radio SFRs owing to sensitivity limitations. Although the frequency range of their observations differs from that used in this study, one possible explanation for our result is that we may be preferentially detecting outliers that are actively star-forming and heavily dust-obscured. Future work with larger samples and consistent multi-band observations will be essential to assess the prevalence and implications of such offsets among FRB host galaxies.

Overall, our results highlight both the promise and the current limitations of using low-frequency radio surveys to identify FRB host galaxies. As survey sensitivity, resolution, and sky coverage continue to improve, the methodologies developed here will serve as a foundation for future, larger-scale analyses of the FRB host population.

6 CONCLUSIONS

In this study, we investigated the host galaxy environments of CHIME/FRBs by cross-matching baseband-localised events with the LoTSS DR2 low-frequency radio source catalogue. Our selection strategy, which does not rely on optical detection, enables the identification of obscured or optically faint star-forming galaxies that may be overlooked by traditional methods.

Among 140 FRBs, 33 were found to lie within the LoTSS footprint, and 16 yielded potential extragalactic radio counterparts. Through multi-wavelength analysis, including photometric and spectroscopic data, spectral energy distribution (SED) fitting, and redshift constraints from the Macquart relation, we identified two secure and one tentative host candidates. All three exhibit signatures of star formation, though $\text{H}\alpha$ -based SFR estimates fall below expectations, likely

due to significant dust attenuation, as supported by infrared colours and compact morphologies.

Our results reinforce the utility of low-frequency radio data in complementing optical searches for FRB host galaxies. Despite the limited sample size and positional uncertainties, our approach demonstrates the potential of radio-based host identification and motivates future follow-up efforts combining deep imaging and spectroscopy to refine host associations and explore the diversity of FRB environments.

Looking ahead, LoTSS DR3 and the full CHIME/FRB baseband catalogue will together provide far greater opportunities to associate FRBs with their hosts. With LOFAR 2.0 offering deeper sensitivity, wider coverage, and sub-arcsecond astrometry, and with next-generation facilities such as CHORD delivering milli-arcsecond localisations, the prospects for robust, large-scale samples of FRB host galaxies are strong. Our pilot study demonstrates that radio continuum imaging can serve as an effective tool for identifying potential host galaxies, even in the absence of immediate optical confirmation. This approach offers a promising framework for future large-scale, statistically robust investigations of FRB environments and progenitors using upcoming radio survey data.

ACKNOWLEDGEMENTS

We sincerely appreciate the anonymous referee’s constructive report on our work. We thank Dr. J.R. Callingham (ASTRON) and Dr. Inés Pastor-Marazuela (API/ASTRON) for their valuable suggestions on this work.

This research has made use of the NASA/IPAC Extragalactic Database, which is funded by the National Aeronautics and Space Administration and operated by the California Institute of Technology. This research has made use of the VizieR catalogue access tool, CDS, Strasbourg, France (DOI : 10.26093/cds/vizier). The original description of the VizieR service was published in 2000, *A&AS* 143, 23. LOFAR data products were provided by the LOFAR Surveys Key Science project (LSKSP; <https://lofar-surveys.org/>) and were derived from observations with the International LOFAR Telescope (ILT). LOFAR ([van Haarlem et al. 2013](#)) is the Low Frequency Array designed and constructed by ASTRON. It has observing, data processing, and data storage facilities in several countries, which are owned by various parties (each with their own funding sources), and which are collectively operated by the ILT foundation under a joint scientific policy. The efforts of the LSKSP have benefited from funding from the European Research Council, NOVA, NWO, CNRS-INSU, the SURF Co-operative, the UK Science and Technology Funding Council and the Jülich Supercomputing Centre. The Liverpool Telescope is operated on the island of La Palma by Liverpool John Moores University in the Spanish Observatorio del Roque de los Muchachos of the Instituto de Astrofísica de Canarias with financial support from the UK Science and Technology Facilities Council.

Y.Z.S. is supported by a Chinese Scholarship Council award at the University of Leicester. RLCS acknowledges support from the Leverhulme Trust grant RPG-2023-240. AR acknowledges funding from the NWO Aspasia grant (number: 015.016.033 and funding from a Consolidator Grant from the Europe research and innovation programme (QuickBlitz, Project number 101170284). Views and opinions expressed are however those of the author(s) only and do not necessarily reflect those of the European Union or the European Research Council Executive Agency. Neither the European Union nor the granting authority can be held responsible for them. The authors

acknowledge early testing of these ideas by Lee Tzabach through an undergraduate project at the University of Leicester.

DATA AVAILABILITY

The CHIME/FRB baseband localisation catalogue used in this study is publicly available at <https://www.chime-frb.ca/catalog>. The LoTSS DR2 radio source catalogue is available at <https://lofar-surveys.org>. Additional multi-wavelength data were obtained from public archives, including the Pan-STARRS and WISE surveys.

REFERENCES

Aggarwal K., Budavári T., Deller A. T., Eftekhar T., James C. W., Prochaska J. X., Tendulkar S. P., 2021, *ApJ*, **911**, 95

Ahn C. P., et al., 2012, *ApJS*, **203**, 21

Ahumada R., et al., 2020, *ApJS*, **249**, 3

Arcus W. R., Macquart J.-P., Sammons M. W., James C. W., Ekers R. D., 2021, *MNRAS*, **501**, 5319

Baker J. G., Menzel D. H., 1938, *ApJ*, **88**, 52

Balasubramanian A., Bhardwaj M., Tendulkar S. P., 2025, *ApJ*, **995**, 51

Bannister K. W., et al., 2019, *Science*, **365**, 565

Becker R. H., White R. L., Helfand D. J., 1995, *ApJ*, **450**, 559

Bernales-Cortes L., Tejos N., Prochaska J. X., Khrykin I. S., Marnoch L., Ryder S. D., Shannon R. M., 2025, *A&A*, **696**, A81

Best P. N., et al., 2023, *MNRAS*, **523**, 1729

Bhandari S., et al., 2020, *ApJ*, **901**, L20

Bhandari S., et al., 2022, *AJ*, **163**, 69

Bhandari S., et al., 2023, *ApJ*, **958**, L19

Bhardwaj M., Lee J., Ji K., 2024a, *Nature*, **634**, 1065

Bhardwaj M., et al., 2024b, *ApJ*, **971**, L51

Bhardwaj M., Balasubramanian A., Kaushal Y., Tendulkar S. P., 2025, *arXiv e-prints*, p. [arXiv:2506.23861](https://arxiv.org/abs/2506.23861)

Bianchi L., Herald J., Efremova B., Girardi L., Zabot A., Marigo P., Conti A., Shiao B., 2011, *Ap&SS*, **335**, 161

Bochenek C. D., Ravi V., Belov K. V., Hallinan G., Kocz J., Kulkarni S. R., McKenna D. L., 2020, *Nature*, **587**, 59

Boquien M., Burgarella D., Roehlly Y., Buat V., Ciesla L., Corre D., Inoue A. K., Salas H., 2019, *A&A*, **622**, A103

Bradley L., 2023, astropy/photutils: 1.8.0, doi:10.5281/zenodo.7946442, <https://doi.org/10.5281/zenodo.7946442>

Brinchmann J., Charlot S., White S. D. M., Tremonti C., Kauffmann G., Heckman T., Brinkmann J., 2004, *MNRAS*, **351**, 1151

Bruni G., et al., 2024a, *arXiv e-prints*, p. [arXiv:2412.01478](https://arxiv.org/abs/2412.01478)

Bruni G., et al., 2024b, *Nature*, **632**, 1014

Bruzual G., Charlot S., 2003, *MNRAS*, **344**, 1000

CHIME/FRB Collaboration et al., 2018, *ApJ*, **863**, 48

CHIME/FRB Collaboration et al., 2021, *ApJS*, **257**, 59

CHIME/FRB Collaboration et al., 2024, *ApJ*, **969**, 145

CHIME/FRB Collaboration et al., 2025, *ApJ*, **993**, 55

Calzetti D., Armus L., Bohlin R. C., Kinney A. L., Koornneef J., Storchi-Bergmann T., 2000, *ApJ*, **533**, 682

Cappellari M., 2012, pPXF: Penalized Pixel-Fitting stellar kinematics extraction, Astrophysics Source Code Library, record ascl:1210.002

Cardelli J. A., Clayton G. C., Mathis J. S., 1989, *ApJ*, **345**, 245

Catalán-Torrecilla C., et al., 2015, *A&A*, **584**, A87

Chang Y.-Y., van der Wel A., da Cunha E., Rix H.-W., 2015, *ApJS*, **219**, 8

Chatterjee S., et al., 2017, *Nature*, **541**, 58

Chen G., Ravi V., Hallinan G. W., 2023, *ApJ*, **958**, 185

Chen X.-L., et al., 2025, *ApJ*, **982**, 203

Chime/Frb Collaboration et al., 2023, *ApJ*, **947**, 83

Chime/Frb Collaboration et al., 2025, *ApJS*, **280**, 6

Condon J. J., Cotton W. D., Greisen E. W., Yin Q. F., Perley R. A., Taylor G. B., Broderick J. J., 1998, *AJ*, **115**, 1693

Cordes J. M., Lazio T. J. W., 2002, *arXiv e-prints*, p. [astro-ph/0207156](https://arxiv.org/abs/astro-ph/0207156)

Cutri R. M., et al., 2013, Explanatory Supplement to the AllWISE Data Release Products, Explanatory Supplement to the AllWISE Data Release Products, by R. M. Cutri et al.

Dolag K., Gaensler B. M., Beck A. M., Beck M. C., 2015, *MNRAS*, **451**, 4277

Dong Y., et al., 2024, *ApJ*, **961**, 44

Draine B. T., Li A., 2007, *ApJ*, **657**, 810

Duncan K. J., 2022, *MNRAS*, **512**, 3662

Eftekhari T., et al., 2025, *ApJ*, **979**, L22

Evans P. A., et al., 2020, *ApJS*, **247**, 54

Faisst A. L., Masters D., Wang Y., Merson A., Capak P., Malhotra S., Rhoads J. E., 2018, *ApJ*, **855**, 132

Fong W.-f., et al., 2021, *ApJ*, **919**, L23

Gajjar V., et al., 2018, *ApJ*, **863**, 2

Ginsburg A., et al., 2019, *AJ*, **157**, 98

Gordon A. C., et al., 2023, *ApJ*, **954**, 80

Graham M., Plante R., Tody D., Fitzpatrick M., 2014, PyVO: Python access to the Virtual Observatory, Astrophysics Source Code Library, record ascl:1402.004

Gürkan G., et al., 2018, *MNRAS*, **475**, 3010

Heintz K. E., et al., 2020, *ApJ*, **903**, 152

Herschel Team et al., 2024, VizieR Online Data Catalog: Herschel/SPIRE point source catalog (HSPSC) (Herschel team+, 2017), VizieR On-line Data Catalog: VIII/12, Originally published in: Herschel catalogs (2017)

Horowicz A., Margalit B., 2025, *arXiv e-prints*, p. [arXiv:2504.08038](https://arxiv.org/abs/2504.08038)

Ibik A. L., et al., 2024a, *ApJ*, **961**, 99

Ibik A. L., et al., 2024b, *ApJ*, **976**, 199

James C. W., et al., 2019, *Publ. Astron. Soc. Australia*, **36**, e009

Kennicutt Jr. R. C., 1998, *ApJ*, **498**, 541

Kennicutt R. C., Evans N. J., 2012, *ARA&A*, **50**, 531

Kennicutt Jr. R. C., Lee J. C., Funes J. G., J. S., Sakai S., Akiyama S., 2008, *ApJS*, **178**, 247

Kewley L. J., Geller M. J., Jansen R. A., Dopita M. A., 2002, *AJ*, **124**, 3135

Kirsten F., et al., 2022, *Nature*, **602**, 585

Kirsten F., et al., 2024, *Nature Astronomy*, **8**, 337

LOFAR2.0 Science Working Group 2023, LOFAR2.0 White Paper (v2023.1), https://www.lofar.eu/wp-content/uploads/2023/04/LOFAR2_0_White_Paper_v2023.1.pdf

Lee-Waddell K., et al., 2023, *Publ. Astron. Soc. Australia*, **40**, e029

Lorimer D. R., Bailes M., McLaughlin M. A., Narkevic D. J., Crawford F., 2007, *Science*, **318**, 777

Loudas N., Li D., Strauss M. A., Leja J., 2025, *arXiv e-prints*, p. [arXiv:2502.15566](https://arxiv.org/abs/2502.15566)

Macquart J. P., et al., 2020, *Nature*, **581**, 391

Magaña Hernandez I., d'Emilio V., Morisaki S., Bhardwaj M., Palmese A., 2024, *ApJ*, **971**, L5

Mannings A. G., et al., 2021, *ApJ*, **917**, 75

Marcote B., et al., 2017, *ApJ*, **834**, L8

Mingo B., et al., 2016, *MNRAS*, **462**, 2631

Mingo B., et al., 2019, *MNRAS*, **488**, 2701

Moroianu A., Wen L., James C. W., Ai S., Kovalam M., Panther F. H., Zhang B., 2023, *Nature Astronomy*, **7**, 579

Moustakas J., Kennicutt Jr. R. C., Tremonti C. A., 2006, *ApJ*, **642**, 775

Niu C.-H., et al., 2021, *ApJ*, **909**, L8

Niu C.-H., et al., 2022, *Nature*, **606**, 873

Núñez C., et al., 2021, *A&A*, **653**, A119

Pleunis Z., et al., 2021, *ApJ*, **911**, L3

Ravi V., et al., 2019, *Nature*, **572**, 352

Salim S., et al., 2007, *ApJS*, **173**, 267

Salpeter E. E., 1955, *ApJ*, **121**, 161

Schawinski K., et al., 2014, *MNRAS*, **440**, 889

Schlafly E. F., et al., 2018, *ApJS*, **234**, 39

Schlegel D. J., Finkbeiner D. P., Davis M., 1998, *ApJ*, **500**, 525

Scholz P., et al., 2017, *ApJ*, **846**, 80

Seebek J., Ravi V., Connor L., Law C., Simard D., Uzgil B., 2021, *arXiv e-prints*, p. [arXiv:2112.07639](https://arxiv.org/abs/2112.07639)

Shah V., et al., 2025, *ApJ*, **979**, L21

Table A1. Data used in the SED fitting for SDSS J114335.11+600334.9

Instrument	Filter	Effective Wavelength (Å)	Flux [†] (mJy)
SDSS	<i>u</i> -band	3546	0.0019±0.0015
	<i>g</i> -band	4670	0.0040±0.0007
	<i>r</i> -band	6156	0.0063±0.0010
	<i>i</i> -band	7472	0.0062±0.0016
	<i>z</i> -band	8917	0.0079±0.0062
WISE	W1	33461	0.0070±0.0018
	W2	45952	0.0062±0.0036

[†] All fluxes have been corrected for Galactic extinction.

Sharma K., et al., 2024, *Nature*, **635**, 61
 Shimwell T. W., et al., 2017, *A&A*, **598**, A104
 Shimwell T. W., et al., 2019, *A&A*, **622**, A1
 Shimwell T. W., et al., 2022, *A&A*, **659**, A1
 Skrutskie M. F., et al., 2006, *AJ*, **131**, 1163
 Smith D. J. B., et al., 2021, *A&A*, **648**, A6
 Spitler L. G., et al., 2016, *Nature*, **531**, 202
 Sudoh T., Linden T., Beacom J. F., 2021, *Phys. Rev. D*, **103**, 083017
 Tang L., Lin H.-N., Li X., 2023, *Chinese Physics C*, **47**, 085105
 Tendulkar S. P., et al., 2017, *ApJ*, **834**, L7
 Vanderlinde K., et al., 2019, in Canadian Long Range Plan for Astronomy and Astrophysics White Papers. p. 28 ([arXiv:1911.01777](https://arxiv.org/abs/1911.01777)), doi:10.5281/zenodo.3765414
 Wang X.-G., Li L., Yang Y.-P., Luo J.-W., Zhang B., Lin D.-B., Liang E.-W., Qin S.-M., 2020, *ApJ*, **894**, L22
 Webb N. A., et al., 2020, *A&A*, **641**, A136
 Yamasaki S., Goto T., Ling C.-T., Hashimoto T., 2024, *MNRAS*, **527**, 11158
 Yao J. M., Manchester R. N., Wang N., 2017, *ApJ*, **835**, 29
 Zhang B., 2023, *Reviews of Modern Physics*, **95**, 035005
 Zhang X., et al., 2023, *ApJ*, **959**, 89
 Zhou R., et al., 2021, *MNRAS*, **501**, 3309
 van Haarlem M. P., et al., 2013, *A&A*, **556**, A2

APPENDIX A: SED FITTING DATA AND RESULTS

We compile multi-wavelength photometry from several surveys. GALEX ultraviolet fluxes are from the AIS catalogue (Bianchi et al. 2011), using the calibrated pipeline fluxes. Optical measurements are obtained from SDSS DR16 (Ahumada et al. 2020), adopting the cModel fluxes. Near-infrared photometry is taken from 2MASS (Skrutskie et al. 2006), using the fluxes derived from the extrapolated profile fits. WISE mid-infrared fluxes are taken from the AllWISE catalogue (Cutri et al. 2013), using values derived from fitting to the imaging maps. Far-infrared measurements from Herschel (Herschel Team et al. 2024), correspond to the average of the TML-derived 250 and 350 μm fluxes over all contributing sources. All data in the table have been corrected for extinction. The photometric measurements originate from surveys with different angular resolutions and photometric methods, and therefore the apertures are not matched across bands. However, the observed spectral energy distribution shows no discontinuities or unphysical jumps, indicating that the fluxes are mutually consistent and can be reasonably compared.

This appendix presents the SED fitting result of the target galaxy using the CIGALE software. The figure below shows the best-fit SED model compared with the multi-wavelength photometric observations.

Table A2. Data used in the SED fitting for SDSS J083444.42+660026.5

Instrument	Filter	Effective Wavelength (Å)	Flux [†] (mJy)
GALEX	FUV	1549	0.2306±0.0140
	NUV	2304	0.3197±0.0110
	<i>u</i> -band	3546	0.2787±0.0064
	<i>g</i> -band	4670	1.0928±0.0010
	<i>r</i> -band	6156	1.9283±0.0010
WISE	<i>i</i> -band	7472	2.6225±0.0010
	<i>z</i> -band	8917	3.2575±0.0283
	<i>J</i>	12319	2.8348±0.0750
	<i>H</i>	16420	3.7904±0.1118
	<i>Ks</i>	21567	2.9201±0.1005
2MASS	W1	33461	1.1981±0.0274
	W2	45952	0.7822±0.0215
	W3	115526	3.9434±0.1526
	W4	220783	6.9022±0.9721
	PMW	2500000	68.2003±11.5000
SPIRE	PSW	3630000	126.7008±9.9000

[†] All fluxes have been corrected for Galactic extinction.

Table A3. Data used in the SED fitting for SDSS J110020.55+595454.4

Instrument	Filter	Effective Wavelength (Å)	Flux [†] (mJy)
SDSS	<i>u</i> -band	3546	0.0010±0.0016
	<i>g</i> -band	4670	0.0225±0.0007
	<i>r</i> -band	6156	0.0511±0.0010
	<i>i</i> -band	7472	0.0757±0.0019
	<i>z</i> -band	8917	0.1039±0.0064
WISE	W1	33461	0.1184±0.0052
	W2	45952	0.0844±0.0089
	W3	115526	0.4998±0.1091
	W4	220783	< 2.3102

[†] All fluxes have been corrected for Galactic extinction.

APPENDIX B: SPECTROSCOPIC ANALYSIS RESULTS

We obtained an optical spectrum of the candidate host galaxy of FRB 20190303B, MCG+11-11-014, using the SPRAT instrument on the Liverpool Telescope. The spectrum shows a clear detection of the H α emission line, which we fitted with pPXF (Cappellari 2012) to estimate its flux.

This paper has been typeset from a $\text{\TeX}/\text{\LaTeX}$ file prepared by the author.

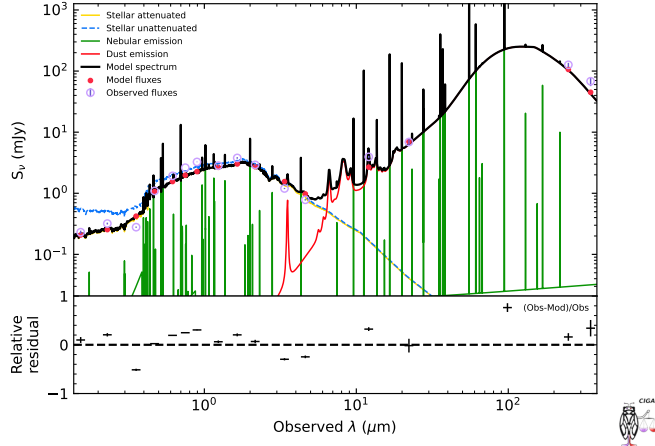


Figure A1. Spectral Energy Distribution (SED) fitting result for the source MCG+11-11-014 using CIGALE. The purple circles represent observed fluxes, the black curve shows the best-fit model, and the red points denote the model flux.

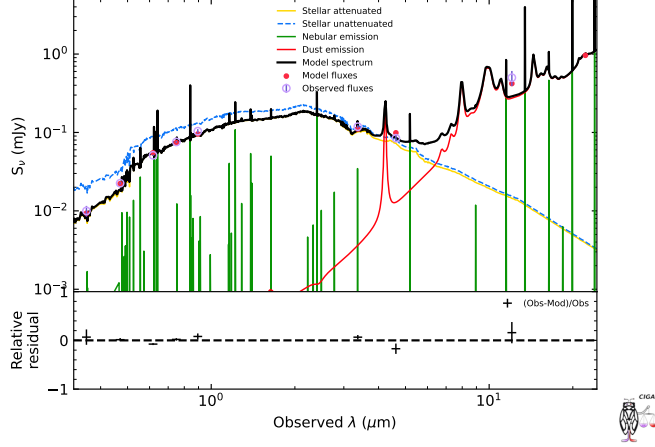


Figure A2. Spectral Energy Distribution (SED) fitting result for the source SDSS J110020.55+595454.4 using CIGALE.

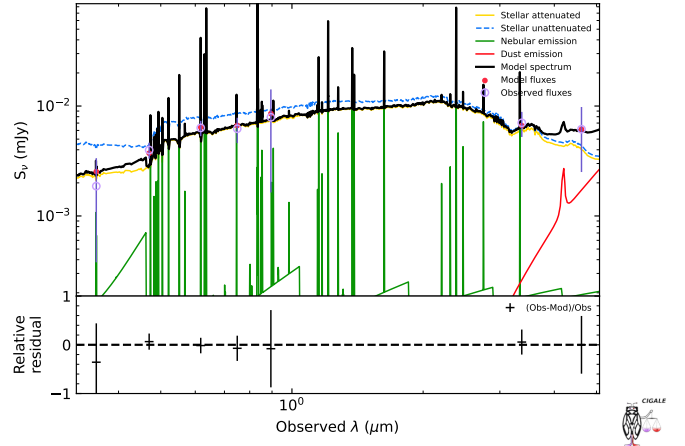


Figure A3. Spectral Energy Distribution (SED) fitting result for the source SDSS J114335.11+600334.9 using CIGALE.

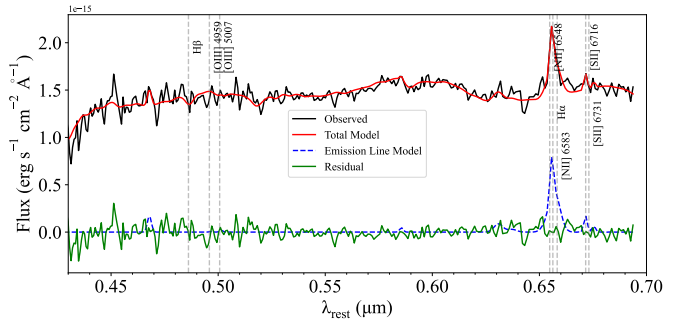


Figure B1. Optical spectrum obtained from the SPRAT instrument on the Liverpool Telescope of the host galaxy candidate MCG+11-11-014 for FRB 20190303B showing a clear detection of the H α emission line. The line is fitted with a single Gaussian profile to estimate its flux, which is later used to derive the star formation rate.